



**Politecnico
di Torino**

Politecnico di Torino

Corso di Laurea Magistrale in AUTOMOTIVE ENGINEERING

A.a. 2023/2024

Sessione di Laurea Novembre 2024

Models of tyre/soft-soil contact for off-road applications

CANDIDATO:

Alberto Buccellato

RELATORI:

Prof. Alessandro Vigliani

Prof. Enrico Galvagno

CORRELATORI:

Dott. Angelo Domenico Vella

Dott.ssa Giulia La Porta

Dott. Luca Zerbato

Abstract

This thesis addresses the interaction between a soft-soil and tire, to enhance the predictions of vehicle performance in diverse off-road conditions. The research begins with a rigorous validation of the solver Optistruct, employed in Finite Element Method (FEM) analyses, and the use of literature tests from the Geotechnical field to ensure precise soil behaviour modelling. To extract parameters for building semi-empirical contact models. This initial stage focuses on accurately capturing soil deformation and stress responses, which are critical for realistic terrain interaction. Building upon these validated soil models, the study explores their application within the automotive research area conducting pressure-sinkage tests. The extracted pressure-sinkage characteristics serve as foundational parameters that can be integrated into vehicle simulation models. By linking these geotechnical insights with vehicle dynamics, the thesis presents a framework for more robust and realistic off-road vehicle FEM simulations, supporting advancements in off-road vehicle design and performance assessment.

Contents

Abstract.....	2
1. INTRODUCTION.....	4
1.1 Bekker study	5
1.2 FEM.....	7
2. Geotechnical tests	12
2.1 Oedometer test	12
2.1.1 Procedure	13
2.2 Triaxial test	16
2.2.1 Mohr-Coulomb failure criterion - parameter evaluation	19
2.2.2 Test procedure	21
3. FE modelling	23
3.1 OptiStruct	23
4. Implementation of the tests.....	29
4.1 Oedometer test	31
4.1.1 Constraints.....	32
4.1.2 Material.....	33
4.1.3 Load	34
4.1.4 Time set up	37
4.1.5 Results	38
4.2 Triaxial test	41
4.2.1 Constraints.....	43
4.2.2 Material.....	44
4.2.3 Load and Enforce displacement	46
4.2.4 Time set up	53
4.2.5 Results	53
4.3 Pressure-Sinkage test.....	58
4.3.1 Boussinesq.....	60
4.3.2 Plate version	63
4.3.3 Pressure sinkage model development	67
5. Conclusion	79
Bibliography	81

1. INTRODUCTION

In the last years, the study of Off-Road vehicle became important, due to the multiple fields in which it belongs, for instance, military, transportation, agriculture. Its main purpose is to predict phenomenon that are different from a classic straight road, due to the complexity of the soil and the presence of variables such, as humidity, grain dimension, cohesion, the behaviour of a vehicle changes a lot.

To simulate the contact and the behaviour of the wheel in this condition, many approaches have been done.

Empirical models: based on laboratory or field test data, use empirical factors retrieved from vehicle measurement, then the model is characterized conducting experiments and follows the fitting of the experimental data curve.

Physics-based models: here the models use physics principles and analytical methods, an example are FEM and DEM methods. This method utilizes high computational power, on the other hand they are more precise.

Semi-empirical models: here are combined empirical formulation with analytical methods to reduce computational power. (Taheri, Sandu, Taheri, Pinto, & Gorsich, 2014)

This thesis aims to bridge the gap between terrain modelling and vehicle simulation in off-road conditions. The research begins by validating the solver used in the Finite Element Method (FEM) analysis, using specific tests of the literature on a sandy soil (La Porta, 2023) to ensure accurate soil behaviour representation. The study then connects these findings to the automotive domain through pressure-sinkage tests, which are fundamental in analysing the interaction between tires and soil. The goal is to extract pressure-sinkage characteristics that can be implemented in various models, enhancing the accuracy of vehicle simulations across different terrains.

The main studies in this field were done by Bekker and Wong, which investigate the contact considering the relationship between pressure and sinkage of a wheel.

The following equation links the kinematics of the wheel to the stress:

$$P = k * z^n \quad (1)$$

In which the P represents the vertical average contact pressure expressed in MPa, k is the soil stiffness contacts for sinkage [MPa/mmⁿ], z is the depth of the sinkage and n is the soil constant related to the soil characteristics.

1.1 Bekker study

The Bekker model, a well-established theoretical framework in geotechnics, plays a crucial role in understanding the interaction between wheeled or tracked vehicles and deformable terrain. Developed by M.G. Bekker in the mid-20th century, this model offers a foundational approach to predicting vehicle performance on soft soils, including sand, clay, snow, and other unstructured terrains. Its core principle revolves around the pressure-sinkage relationship, which characterizes how soil deforms under load and, consequently, how vehicles penetrate and mobilize on various ground surfaces. Bekker views wheels and tracks as basic loading surfaces with similar shapes but varying in length and width (*Figure 1*).

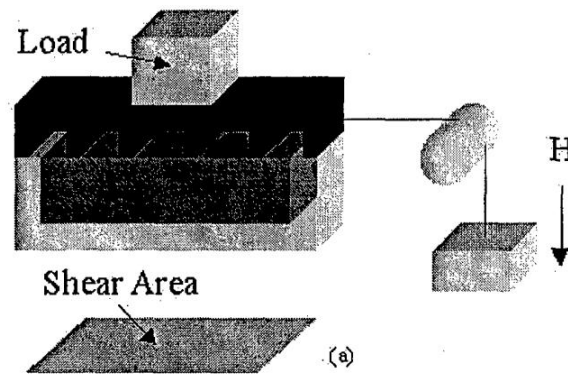


Figure 1 (Laughery, 1990)

In his tests, Bekker used a load with a defined geometry to measure and analyse the shear area generated as a block moves relative to the soil. His goal was to determine

the maximum shear strength, which is not achieved immediately. Instead, the soil must undergo a certain degree of compaction before it reaches a steady-state mechanical shearing stress (Laughery, 1990). Shear stress is defined as the ratio between the vehicle's tractive force, which acts parallel to the soil surface, and the area of the block that is perpendicular to the surface. During the shearing process, the tractive force is opposed by the soil's resistance, while moving across the terrain (Laughery, 1990). The normal load, that can be the load of a vehicle itself generates ground pressure, that will compact the soil and alters the soil resistance.

The shear stress and ground pressure are analysed using the Mohr-Coulomb criterion (*Equation 2*) to determine when soil failure occurs. The shear strength of the soil is defined as the maximum value of shear stress that can be sustained before the soil yields. In this analysis, the Mohr's circle expands to a critical point before failure, and once failure occurs, the failure line is established. The equation of this line,

$y = mx + b$, allows for the calculation of key soil properties, such as the cohesion coefficient c , represented by b , and the friction angle ϕ , denoted as m (Laughery, 1990). These parameters are crucial in understanding the soil strength to shearing forces.

$$\tau' = c' + \sigma' \tan \phi' \quad (2)$$

BDTM, Bekker's derived terramechanics model, is a simple, linear one-degree-of-freedom model representing the load's linear effect on the soil. The original formulation of the model was created in a spreadsheet format and is based on three main groups of input parameters (Laughery, 1990). The first group consists of vehicle specifications, including dimensions and weight. The second group focuses on the vehicle's performance on specific terrains, while the third group is used to calculate the WES (Wheel Efficiency System) mobility index, this index is used to evaluate the mobility performance of vehicles, particularly in off-road and challenging terrains.

Instead, the outputs are organized into seven categories, allowing for a systematic evaluation of sinkage in both frictional and cohesive soils. To facilitate this analysis, Bekker derived a formula from his bavameter, which provides a mathematical basis for predicting sinkage behaviour in these different soil types (Laughery, 1990).

$$z = \left[\frac{p}{\frac{k_c}{b} + k_\phi} \right]^{1/n} \quad (3)$$

In this formula, p represents the ground pressure, b denotes the width of the track or tire, K_c and K_ϕ are the cohesive and frictional moduli of soil deformation, respectively, while n is the exponent that characterizes the soil's deformation behaviour (Laughery, 1990).

1.2 FEM

With the increased computational power of personal computers, tools like the Finite Element Method (FEM) have become fundamental for studies of this kind, providing critical insights and accurate simulations needed to understand complex interactions and behaviours. These tools allow researchers to analyse detailed material responses, structural integrity, and the effects of varying conditions, making them invaluable for advancing knowledge in fields that rely on precision and reliability. Furthermore, FEM helps reduce the cost of physical equipment needed for specific tests, while expanding the range of potential experiments. It allows researchers to simulate an infinite variety of scenarios, including testing varied materials, even rare ones, if their mechanical properties are defined correctly. Additionally, it enables the exploration of complex geometries that might be challenging to obtain or time-consuming to test physically. As a result, FEM is a powerful tool that introduces flexibility and efficiency into the research process.

Significant work has been done in this field, with one of the most notable studies conducted by Fevers, who investigated how the components of a wheel transmit load using an air-filled model (Fevers, 2004). His research utilized a 2D FEM model. Unlike traditional 2D tire models, which often seek a mathematical description of the tire's overall response, Fevers' model focuses on mechanically reproducing the tire's basic components (*Figure 2*). Fevers opted for a 2D model over a 3D one due to the significant computational effort required for 3D simulations. Transferring the soil model into the 2D space in FEM is straightforward. However, existing 2D tire models are not satisfactory for tire-soil interaction in FEM, as most of them do not account for soil deformation or accurately reproduce the deformation of the air-filled tire (Fevers, 2004). In his study, the carcass is the only component significantly influenced by deformation in the third dimension. Thus, creating an effective 2D model of an air-filled tire requires developing an appropriate representation of the carcass. Therefore, the most challenging aspect of this approach was accurately modelling the tire carcass. Simulation results from this new tire model, tested on both even and uneven surfaces, were compared to actual test results, demonstrating the model's capabilities. Additionally, further simulations explored the effect of reduced tire inflation on soft soils, highlighting how different soil types respond differently under these conditions (Fevers, 2004).

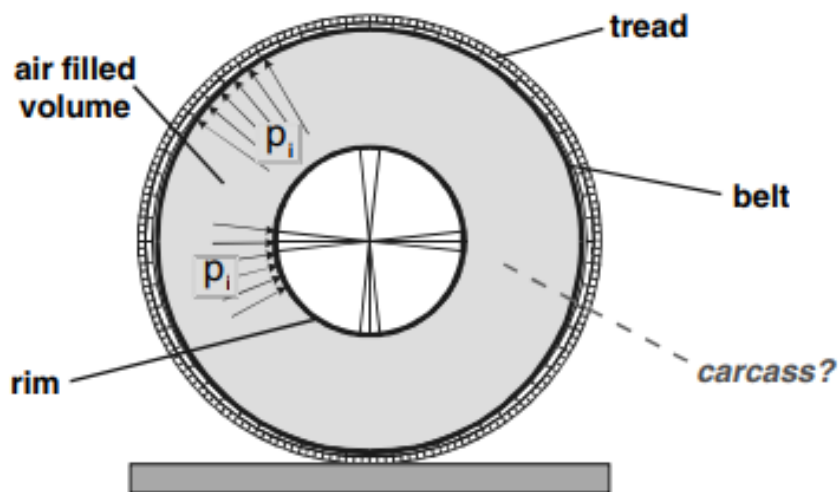


Figure 2: Element of the tire in 2-D (Fevers, 2004)

In the following years, the implementation of 3D models became the preferred approach for this type of simulation, thanks to the increasing computational power of contemporary computers. A significant contribution in this field was made by N. Moslem and G. Hossein (Moslem & Hossein, 2014), who conducted a detailed study using a three-dimensional finite element model. Their research focused on the interaction between a 115/60R13 radial tire, with moderate tread, and soil.

Their model was validated by comparing its results with data from experimental tests, demonstrating that numerical simulations can serve as reliable tools for predicting soil compaction and stress fields. In their work, the tire was modelled using SolidWorks Simulation to accurately represent its structural components (*Figure 3*). The strain energy stored in the tire rubber was calculated using the Mooney-Rivlin equation, a well-known approach for modelling hyper-elastic materials (Moslem & Hossein, 2014).

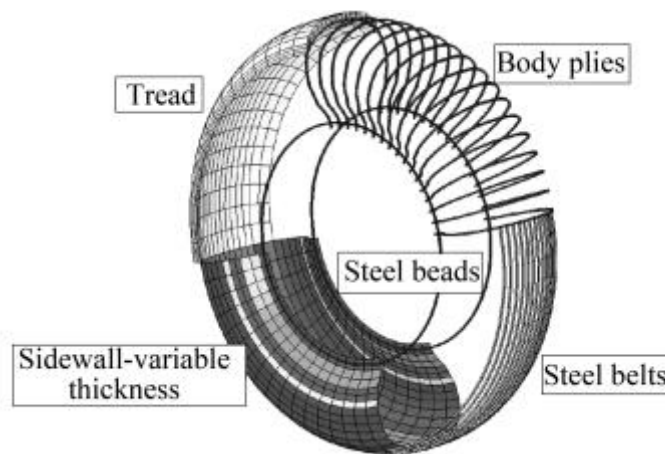


Figure 3: Radial tire components modelled in Solidworks (Moslem & Hossein, 2014)

To simulate soil compaction, they employed the Drucker-Prager yield criterion, which is commonly used for materials like soil that exhibit pressure-dependent yielding behaviour. This combined approach allowed for a robust and accurate representation of tire-soil interaction.

To model the soil, they ensured that the boundaries were set far enough from the tire's location to avoid border effects influencing the results. The volume representing the soil was divided into two regions with different mesh densities: a denser mesh near the tire, where contact interactions were critical, and a less dense mesh in the lower region (*Figure 4*) (Moslem & Hossein, 2014). This approach was chosen to optimize computational efficiency by reducing storage requirements and shortening simulation time, while still maintaining accuracy in the areas where precision was most needed.



Figure 4: 3-D mesh model tire/soil (Moslem & Hossein, 2014)

Li Z., Chen W., Li Y. and Wu W. conducted a study utilizing a three-dimensional finite element tyre–pavement contact model developed in ABAQUS. This model was applied to investigate the interaction between different simplified pavement types and a rolling or braking tyre, with a particular focus on analysing pavement skid resistance. Their findings revealed that, under steady-state rolling conditions, the peak contact stress on the simplified pavement increased as the mean texture depth of the pavement rose, while the contact area simultaneously decreased (Li, Chen, Li, & Wu, 2023).

The tire model was designed to replicate a 175/80 R14 radial tire, with the neo-Hookean model applied to simulate the rubber material and a linear elasticity model used for the cord skeleton (Li, Chen, Li, & Wu, 2023). The construction of the tire's 3-D model followed a step-by-step process: initially, a 2-D profile of the tire was created, then this profile was rotated to generate a 3-D model of half the tire. In the final step, the half-tire model was mirrored to produce the complete 3-D tire model (Figure 5).

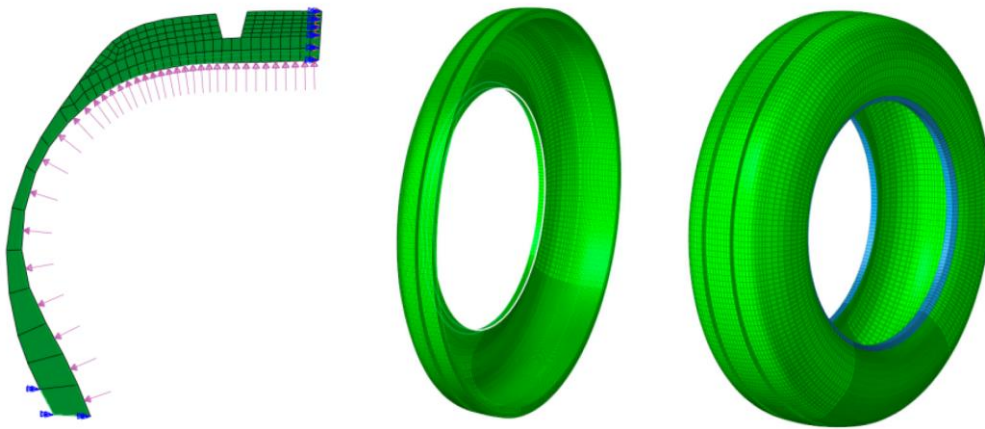


Figure 5: Steps of production of 3-D tire model (Li, Chen, Li, & Wu, 2023)

The soil model was initially created in a 3-D modelling software and subsequently analysed in ABAQUS. To represent various aggregate grains, hemispherical shells of different diameters were used, with the size of each shell corresponding to the specific grain size (Figure 6).

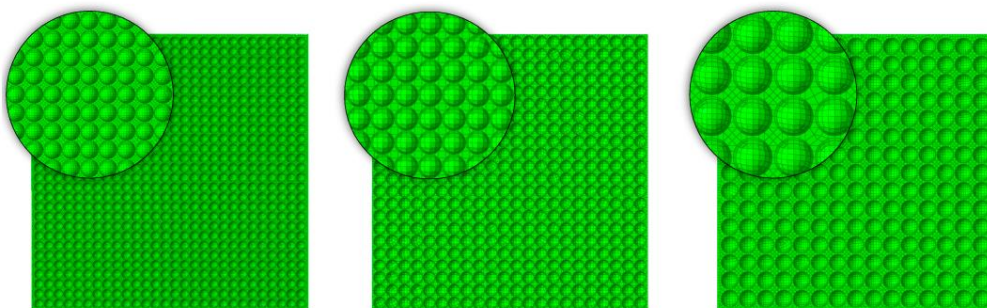


Figure 6: Soil model with different aggregate grains dimension (Li, Chen, Li, & Wu, 2023)

2. Geotechnical tests

To accurately simulate soil behaviour, the first crucial step is to calibrate the model so that it closely aligns with experimental data, aiming to achieve the most realistic response possible.

In geotechnical engineering, certain tests are essential for characterizing the diverse properties of various soil types. Among these, the oedometer and triaxial tests play a fundamental role. The oedometer test is primarily used to determine the soil's compressibility and consolidation properties, providing insights into how the soil will settle under load over time. On the other hand, the triaxial test offers a more comprehensive view of soil strength, allowing for the analysis of shear strength, under different stress conditions.

The work will focus on oedometric and triaxial tests, toward a deeper understanding of the mechanical behaviour of soils, and how different terrains respond to loading.

2.1 Oedometer test

The oedometer test is used to determine the behaviour of the soil under various one-dimensional load conditions. This laboratory test provides valuable insights into the compressibility of soil, helping engineers to predict how a soil layer will respond when subjected to vertical loads. This test is particularly crucial for projects where settlement and stability are of paramount concern, as it enables the calculation of parameters like the compression index and coefficient of consolidation. The inventory of an oedometer laboratory includes usually a bench, the oedometer itself, the shell in which the test material is contained, the measurement system and a weight set. Figure 7 shows the oedometer device.



Figure 7: Oedometer, <https://www.geo-con.com.au> (Consolidation System Front Loading Oedometer, s.d.)

2.1.1 Procedure

The material sample is confined into a metal ring called consolidation shell (*Figure 8*), that does not allow lateral deformation; therefore, radial strain is zero. Usually, the test is conducted on a saturated sample, to analyse typical field conditions of soils, especially cohesive soils (such as clays), where the water in the soil pores significantly affects the mechanical behaviour. Typically, the diameter to height ratio is 2-3, therefore the diameter is 2-3 times the height of the ring. In the experiments reported in this thesis (La Porta, 2023) the ring has a standard dimension of 50.46 mm in diameter and 20 mm in height.



Figure 8: Consolidation shell (Consolidation System Front Loading Oedometer, s.d.)

On the top and bottom of the sample porous stone is placed, to allow drainage of water in the solicited dimension, the axial one. The sample is subjected to an incremental axial load as reported in Table 1. The load is applied in stages by adding or removing the weights (Adamo, et al., 2017).

Table 1: Loading and unloading steps of a oedometric test (La Porta, 2023)

SIGMA [kPa]
0
12.3
24.5
49
98.1
196.1
392.3
784.5
1569.1
392.3
98.1
24.5

The results of the oedometer test are typically presented in the form of graphs and equations that describe the soil's compressibility and consolidation characteristics. One of the most important is the consolidation curve $e-\log \sigma_v$ (Figure 9): this graph

provides insight into the compressibility of the soil under loading and unloading conditions.

In the $e-\log \sigma$ graph, three parts can be distinguished:

1. Initial consolidation (recompression curve): represents the behaviour of the soil when it is first loaded, usually in this part the material remains in the linear-elastic region, the slope of this section is not very steep and gives information of the recompression index C_r .
2. Virgin compression curve (normally consolidated zone): when the applied stress exceeds the soil's pre-consolidation pressure, the soil enters in the normally consolidated state, where it compresses more importantly under additional stress. The slope of this portion is steeper, and it's called compression index C_c (Lancellotta & R., 2012).
3. Unloading and reloading (unloading-reloading curve): during unloading, the soil recovers part of the deformation elastically, but a portion of the deformation remains irreversible due to the material's plastic behaviour. During reloading, the soil initially follows the unloading path, exhibiting elastic behaviour, until it reaches the preconsolidation pressure. Beyond this point, the soil re-enters the normal compression phase

The compression index represents the void ratio variation due to load increments:

$$C_c = \frac{\Delta e}{\Delta \log \sigma} \quad (4)$$

Where Δe is the change in void ratio and $\Delta \log \sigma$ represents the effective normal stress variation.

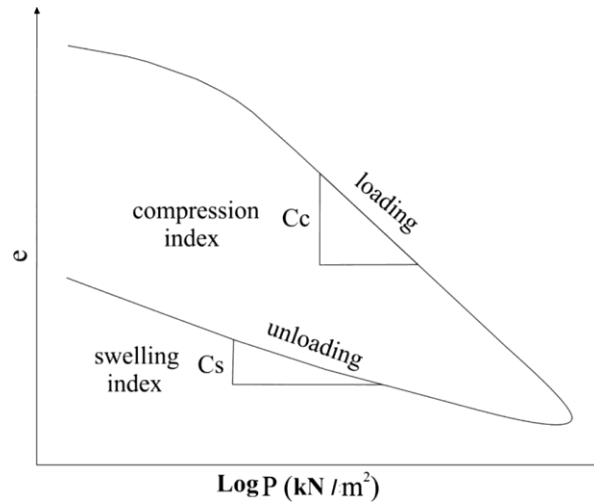


Figure 9: Typical consolidation curve (Aldaood, 2022)

To measure the axial displacement a LVDT (Linear Variable Displacement Transducer) is used. Then the axial strain is calculated, and therefore the consolidation curve.

2.2 Triaxial test

The triaxial test is one of the most used tests for laboratory soil mechanics characterisation, specifically to determine the shear strength and stiffness of a material. This test is chosen over the direct shear stress, because the triaxial device allows the sample drainage and the control and measurement of pore water pressures. Through this test, the resistance parameter of the Mohr-Coulomb failure criterion (Figure 10, equation 5), and the Young's modulus E may be determined.

$$\tau' = c' + \sigma' \tan \phi' \quad (5)$$

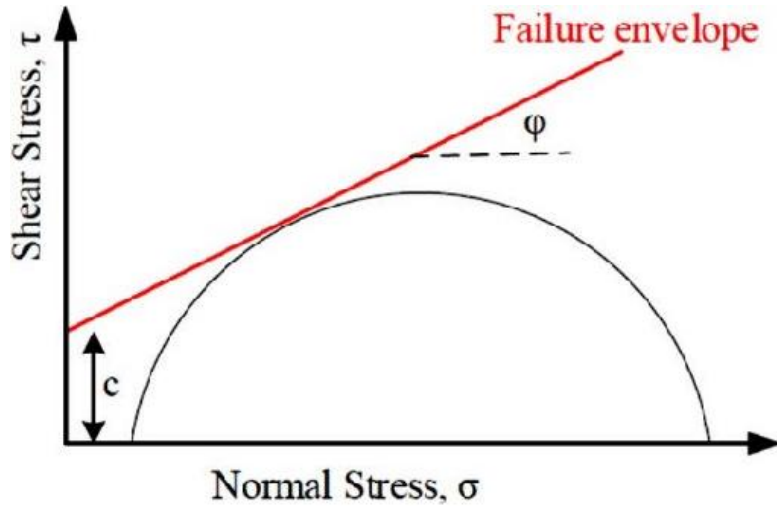


Figure 10: Mohr-Coulomb failure criterion (Giwangkara, 2020)

In equation 5, ϕ' is the friction angle and c' is the cohesion of the material. The tests used in this thesis to validate the developed model (La Porta, 2023) see cylindrical samples of 70 mm in diameter, and 140 mm in height. Generally, the standard test consists of two main phases (out of the first saturation step of the sample): consolidation phase, consisting on the application of a isotropic confining stress σ_c , to simulate the in-situ stresses; shear phase, during which an axial stress σ_a , is applied through a mechanical press, while the radial stress is maintained constant. Their difference is the deviatoric stress q :

$$q = \sigma_1 - \sigma_3 = \sigma_a - \sigma_c \quad (6)$$

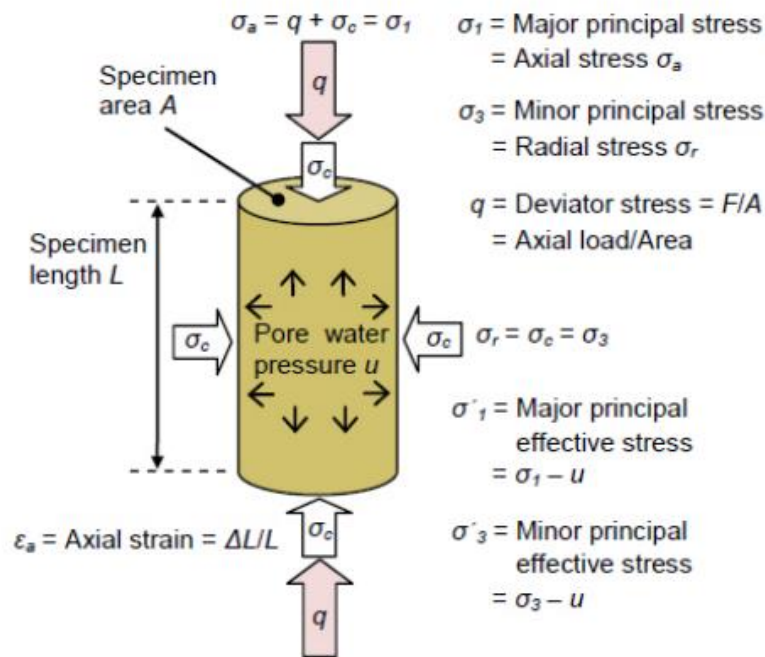


Figure 11: Stress state during triaxial test (GDS instruments, s.d.)

There are three main types of triaxial test:

1. Unconsolidated undrained test (UU): fast and simple procedure, for short term soil stability. During this test, consolidation is not performed, and drainage is not allowed during shear;
2. Consolidated drained test (CD): describe long-term loading response, providing the strength parameters. This is the most complete one, including consolidation phase and drained conditions during shear;
3. Consolidated undrained test (CU): it allows strength parameters to be determined based on the effective stresses whilst permitting a faster rate of shearing compared to CD test. (Lancellotta & R., 2012)

The tests reported here (La Porta, 2023) are CID, i.e. consolidated isotropically drained tests.



Figure 12: Triaxial Test Machine (Triaxial Test Machine, UU Test System, s.d.)

2.2.1 Mohr-Coulomb failure criterion - parameter evaluation

To determine the material characteristics through the triaxial test using the Mohr-Coulomb criterion, data obtained from the test are firstly analysed. It is important to note that the material's response varies with the confining pressure, as this directly influences the material's deformation and strength properties.

The shear strength of a material tends to increase with higher confining pressure. This effect is explained by the Mohr-Coulomb theory, which describes shear strength as a function of the material internal cohesion and friction angle.

With higher confinement, the material can withstand greater deformation before breaking, as the additional pressure interferes with the propagation of internal fractures or particle movement that could lead to failure.

The Critical State Line represents the state at which the soil cannot sustain any additional load without undergoing continuous deformation. By plotting deviatoric stress q and effective stress p' (Equation 7, u represent pore fluid pressure) on a $q -$

p' diagram, the line is composed by plotting peak values for three tests under different confining pressures. The line interpolated through these three points provides the information needed to calculate ϕ the friction angle and c the cohesion.

$$p' = \frac{(\sigma_1 - u) + 2(\sigma_3 - u)}{3} \quad (7)$$

Knowing the slope m of this line, ϕ can be calculate using the following equation:

$$m = \frac{6 \operatorname{sen} \phi}{3 - \operatorname{sen} \phi} \quad (8)$$

By determining the intercept of this line, the cohesion can be estimate using the equation below:

$$c = q_c \frac{1 + 2K_a}{6\sqrt{K_a}} \quad (9)$$

With q_c corresponding to the intercept value of the critical state line and K_a as the active earth pressure coefficient expressed as follows:

$$K_a = \frac{1 - \operatorname{sen} \phi}{1 + \operatorname{sen} \phi} \quad (10)$$

The active earth pressure coefficient helps evaluate the pressure exerted by a soil on retaining structures (such as retaining walls) when the soil expands or deforms freely, reaching an active limit equilibrium condition. It represents the ratio of horizontal (lateral) pressure to vertical (normal) pressure acting on the principal plane of stress when the soil is free to expand laterally.

2.2.2 Test procedure

A cylindrical sample is used, the height-to-diameter ratio is usually 2:1, and the diameter may vary from 38 mm to 100 mm. The soil is confined with a rubber membrane (*Figure 13*), confined between the bottom and the top of the triaxial cell. Then, the triaxial device consists of a plexiglass cell, to confine the sample with a fluid through which the radial pressure is applied, usually water. The rubber membrane separates the soil sample from the cell fluid.



Figure 13: Prepared sample for the test (Triaxial testing, 2021)

The test consists of three main phases:

1. SATURATION
2. CONSOLIDATION
3. FAILURE

1. Saturation

In this phase a σ_c isotropic effective pressure is applied onto the sample. After a first phase, called *flushing*, which consists of the passage of de-aired water into the sample driven by a hydraulic gradient, saturation is achieved through gradually increasing cell and pore pressures, and maintaining a constant isotropic effective stress. For more details on the introduced procedure, the author refers to La Porta, 2023.

2. Consolidation

The consolidation phase is carried out to bring the specimen to the desired effective stress condition for the shearing process. This is usually achieved by raising the cell pressure while keeping the pore pressure constant (and so increasing the effective pressure). To analyse this phase, the same graph used for the Oedometer test is used, the consolidation curve (*Figure 9*).

3. Failure

In the case of shear at strain control, the soil is sheared by applying a constant axial strain rate through upward (compression) or downward (extension) movement of the base of the triaxial cell, driven by a mechanical or hydraulic system. The rate of axial strain, along with the sample drainage condition, is dependent on the type of triaxial test being performed, and the soil tested. Usually, the test is interrupted when the axial strain reaches the 20%. The results can be analysed through a stress-strain curve (*Figure 14*) in which can be identify yield point and the failure point.

The axial loading during the shear phase can be applied in two different ways, in *strain-control* or *stress control*. In the first approach a constant rate of strain (displacement rate) is applied, and the corresponding stresses are measured. Instead in the second one the axial stress is increased, and the strain observed.

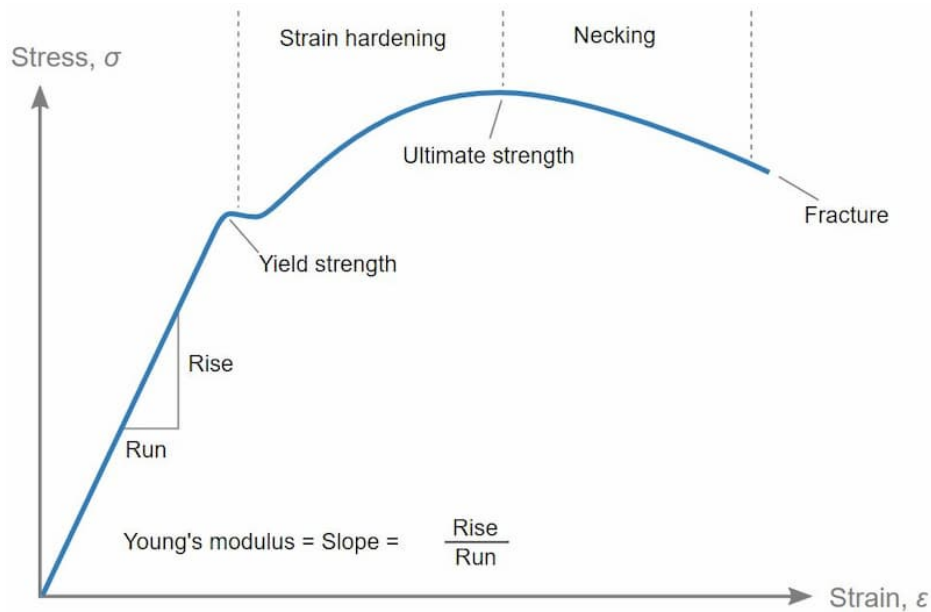


Figure 14: Generic stress-strain curve (Velling, 2020)

3. FE modelling

To develop the finite element model for reproducing the following tests, the software HyperMesh is used. This tool allows us to create solids, generate meshes, and set all the parameters required for the simulation. Once the model is prepared, the simulation file will be provided to the OptiStruct solver, which will be used to run the simulation.

3.1 OptiStruct

OptiStruct is the solver used to perform the tests. The solver has been first introduced in 1994 and now widely recognized as a powerful and reliable tool.

The main challenge with this solver lies in its different field of application. This solver is traditionally designed for structural simulations, making it quite distinct

from applications in the terrain and soil domain. A more specialized soil or ground solver, however, would inherently account for critical aspects specific to soil behaviour, which are crucial in geotechnical contexts.

For example, OptiStruct cannot replicate the saturation phase in a triaxial test because it does not account for material porosity. In contrast, a geotechnics solver includes this by default.

OptiStruct typically supports linear and nonlinear analyses, with a focus on topology optimization and mechanical component design. It is capable of handling static, dynamic, and fatigue analyses.

In this study, an elastoplastic material was chosen to model the soil in the initial iteration. The material definition combines two cards, *MAT1* and *MATSI*, which account respectively for elastic and plastic deformation. This specific combination was selected to accurately represent the plastic behaviour characteristics of the soil.

To model the linear isotropic properties of a material, the *MAT1* card is used. This card is used for its simplicity and effectiveness in representing materials that exhibit elastic, isotropic behaviour.

In this card, various parameters can be specified, as in figure 15.

Card Image:	≡	MAT1	▼
User Comments:		Hide In Menu/Export	▼
E:			
G:			
NU:			
RHO:			
A:			
TREF:			
GE:			

Figure 15: *MAT1* Card, screenshot

Here the description of the parameters:

- E , Young's modulus;
- G , Shear modulus;
- ν , Poisson's ratio ν ;
- RHO , Mass density;
- A , Thermal expansion coefficient;
- $TREF$, Reference temperature for thermal loading;
- GE , Structural element damping coefficient.

To simulate stress-dependent material properties in applications involving nonlinear materials, a key tool in OptiStruct is the *MATS1* card (Figure 16).

MATS1:	<input checked="" type="checkbox"/>
TID:	<input type="text"/>
TYPE:	<input type="text"/>
H:	<input type="text"/>
YF:	<input type="text"/>
HR_REAL:	<input type="checkbox"/>
HR:	<input type="text"/>
LIMIT1:	<input type="text"/>
TYPSTRN:	<input type="text"/>
MC:	<input type="checkbox"/>
LDP:	<input type="checkbox"/>

Figure 16: *MATS1* Card, Screenshot

Follows a description of the parameters:

- TID , Specify the curve between stress and strain;
- $TYPE$, Material nonlinearity type;
- H , Work hardening slope, allow the introduction of hardening;
- YF , Yield function criterion;

- *HR*, Hardening Rule, specify the type of hardening;
- *LIMIT1*, Initial yield point;
- *TYPSTRN*, Specifies the type of strain used on the x-axis of the table pointed to by TID;
- *MC*, To activate the Mohr-Coulomb plasticity model;
- *LDP*, To activate Linear Drucker-Prager plasticity model.

This card allows for the specification of nonlinear material characteristics, particularly related to plasticity and elasto-plasticity.

Different types of nonlinearities are considered in analysis, including geometric nonlinearity, material nonlinearity, and contact analysis:

1. **Geometric Nonlinearity:** This accounts for changes in geometry as a structure deforms, impacting the formulation of constitutive and equilibrium equations. Many engineering applications require large deformation analysis to accurately represent the structural response under significant displacements and rotations.
2. **Material Nonlinearity:** This type addresses the nonlinear behaviour of materials, which depends on factors like current deformation, deformation history, deformation rate, temperature, and pressure. Material nonlinearity is essential for capturing complex material responses under various loading conditions.
3. **Contact Analysis:** This involves analysing interactions between different bodies or parts of a structure, where contact conditions change dynamically based on the load and deformation.

Each of these nonlinearities plays a critical role in achieving realistic simulations for advanced engineering applications.

Within the *MATSI* card, various parameters can be defined, such as material hardening, which is essential for plasticity analysis. For the *MATSI* card to function correctly, the associated *MAT1* card must also be specified, as it defines the linear elastic behaviour of the material.

The *MAT1* card is used to define the linear-elastic portion of the material response. For the *MATSI* card, the following parameters are specified:

- $H = 0$: This sets the material to perfectly plastic behaviour, with no hardening after yield.
- Yield Function Criterion: Defines the criterion for yielding.
- Yield Point: Specifies the stress at which the material begins to yield.
- Strain Type (*TYPSTRN*): Determines the type of strain used in the material's stress-strain relationship:

TYPSTRN = 0: Converts the stress vs. total strain relationship.

TYPSTRN = 1: Converts the stress vs. plastic strain relationship.

These settings ensure that the material behaves as linear-elastic until the yield point, after which it deforms plastically without additional hardening.

The Mohr-Coulomb plasticity criterion was introduced in the 2023 release of the solver, specifically for materials such as soils and rocks, where frictional and dilatational effects are significant. In these materials, plastic behaviour depends heavily on hydrostatic pressure, as internal friction is proportional to the normal force applied.

To implement this plasticity criterion, the *MAT1* and *MATSI* cards are required. In this setup, the *MATSI* card is used solely to define the Mohr-Coulomb parameters (*Table 2*). However, testing has shown that the solver does not rely directly on parameters set within *MATSI* to dictate material behaviour. Instead, it uses the Mohr-Coulomb criterion parameters to evaluate the material's response.

This approach ensures that the material's frictional characteristics and pressure-dependency are accurately represented in the model, critical for simulating the realistic behaviour of soils and rocks under various load conditions.

Table 2: MC parameters

COHE	Cohesion	value
FRICA	Friction angle	Real ≥ 0.0 and ≤ 89.9
DILA	Dilatancy angle	Default = FRICA or Real ≥ 0.0 and \leq FRICA

Nonlinear failure criteria, such as Mohr-Coulomb, are more challenging to solve under direct loading conditions because the solver must manage stress increases that may exceed the material's limits at certain points, causing divergence.

One potential solution is to reduce load increments by using a gradual loading strategy with smaller load steps. However, after testing, tests shows that the best approach is to use an enforced displacement. This configuration proved to be the most effective, and it was ultimately the one chose for our test.

Yield Criteria used by the MC plasticity model:

$$f = \sigma_1 - \sigma_3 + (\sigma_1 + \sigma_3)\sin\phi - 2c \cos\phi \leq 0 \quad (11)$$

Where:

- σ_1 and σ_3 are the maximum and the minimum principal stress of a stress state;
- c , Cohesion;
- ϕ , Friction angle.

In the Mohr-Coulomb criterion, the *flow rule* describes how a material, such as soil or rock, deforms plastically once it reaches its yield point. While the Mohr-Coulomb yield criterion defines the conditions under which the material begins to yield, the flow rule establishes the direction and magnitude of plastic deformation that occurs after yielding.

The flow rule is particularly important for geotechnical materials, as they often exhibit dilatancy, a volumetric expansion that occurs when they are subjected to shear stress. This behaviour is typical of granular materials, such as sand and gravel, which tend to expand as they are sheared. In these materials, particle rearrangement and interaction under shear stress led to an increase in volume.

Flow rule:

$$g = \sigma_1 - \sigma_3 + (\sigma_1 + \sigma_3) \sin \varphi \quad (12)$$

Where φ is the dilatancy angle. It represents the material's tendency to expand volumetrically during plastic deformation under shear stress. A higher dilatancy angle indicates a greater degree of volumetric expansion during plastic deformation.

In practical applications, an unrealistic dilation angle can lead to an overestimation of soil or structural stability.

In associated flow models, the dilation angle matches the internal friction angle, meaning the direction of plastic deformation follows the yield criterion. This often results in an overestimation of dilation in many simulations. In non-associated flow models, however, the dilation angle can be defined independently from the friction angle. This approach allows for greater control over dilation, improving accuracy for materials that do not expand significantly, such as clays.

4. Implementation of the tests

This chapter will discuss about the implementation of the developed models:

- Oedometer test model;
- Triaxial test model;
- Pressure sinkage test model.

It's importance to clarify that the Geotechnical tests models were validate through experimental data from (La Porta, 2023), in which a sand of Fontainebleau. The

grains have diameters ranging from 0.063 mm to 0.25 mm, which classifies it as fine sand.

Here in the following table 3, there are listed the dimensions of the sample for each test performed in the thesis (La Porta, 2023):

Table 3: Sample dimensions of the thesis (La Porta, 2023)

	DIAMETER	HEIGHT	
OEDOMETER TEST	50.46	20	mm
TRIAXIAL TEST	70	140	mm

To validate, the FEM model the following figures are used.

- The first one (*Figure 17*), representing the consolidation curve;
- The second (*Figure 18*), representing the critical state line;
- The third (*Figure 19*), representing the stress-strain curve for different consolidation pressure.

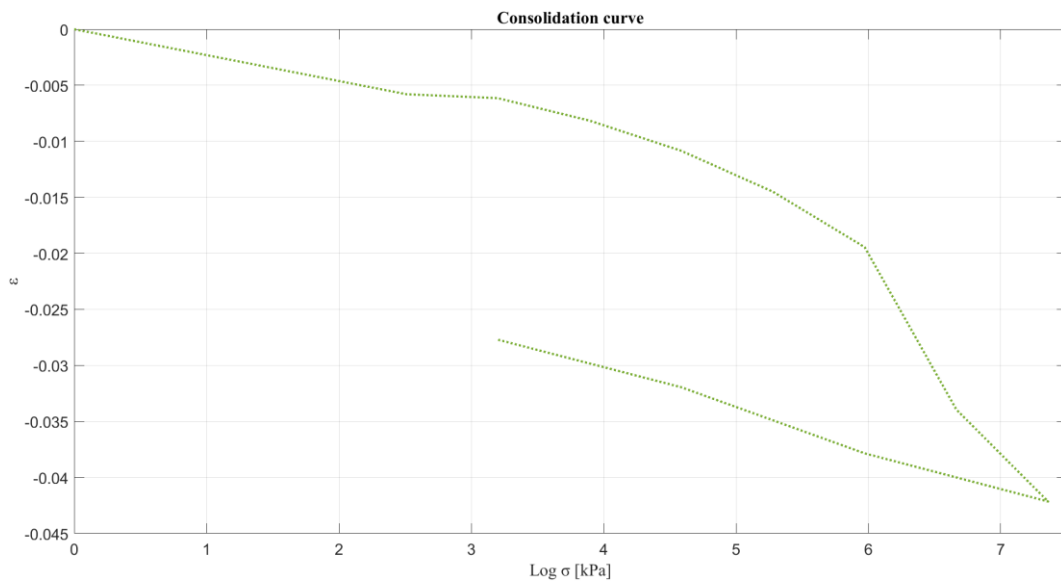


Figure 17: Consolidation curve, experimental data

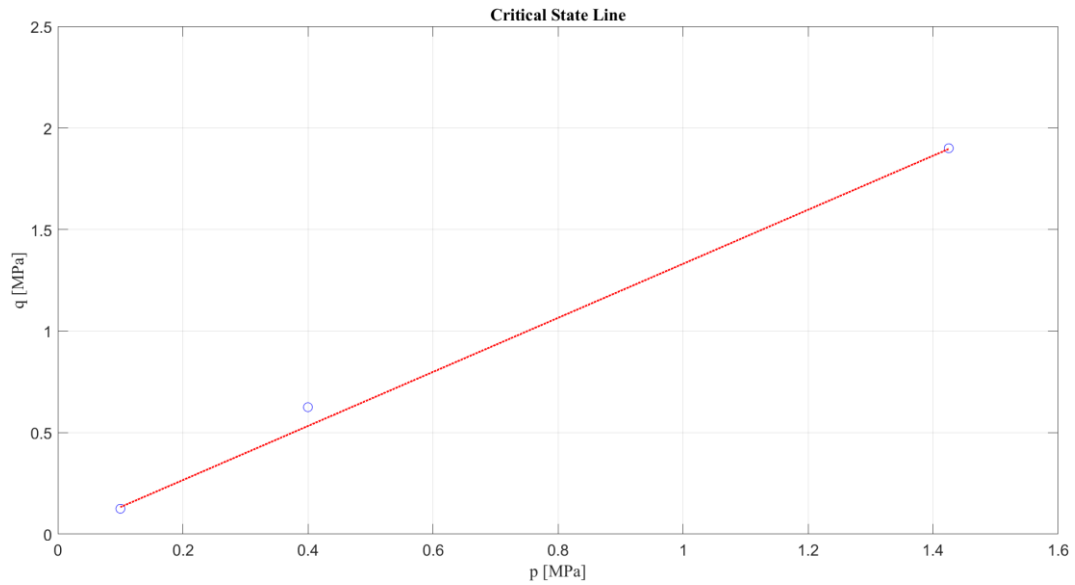


Figure 18: Critical State Line, experimental data

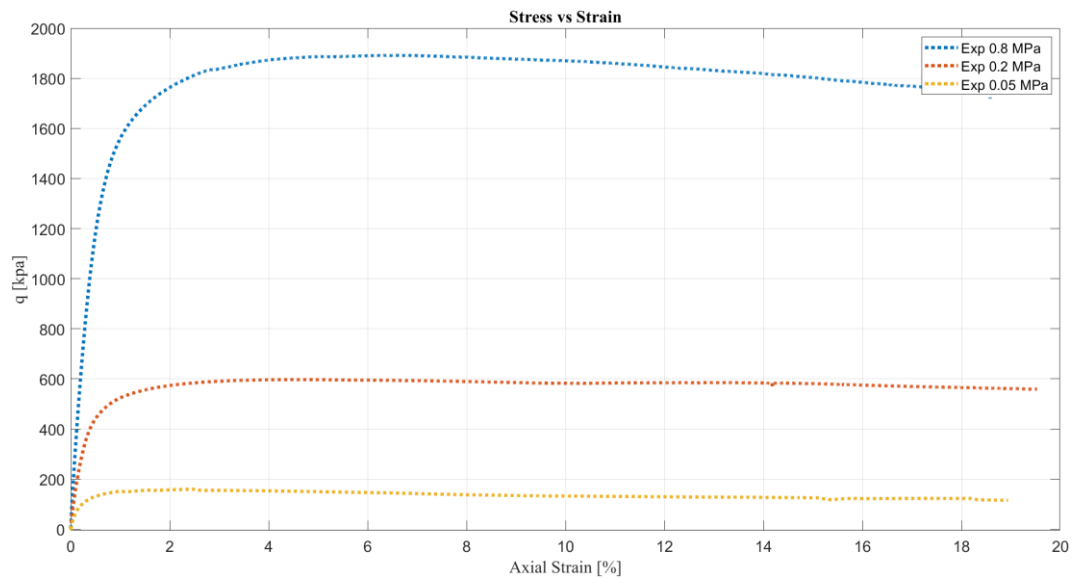


Figure 19: Stress-Strain, for different consolidation pressure, experimental data

4.1 Oedometer test

Starting from the data provided by the experimental oedometer test, the modelling process is initiated using the Altair HyperMesh preprocessor.

First, the geometry for the cylindrical sample used in the test needs to be created. As discussed in Chapter Two, the test follows standard dimensions; for this

simulation, a cylinder with a diameter of 50 mm and a height of 19 mm is chosen (*Figure 20*). Generating the cylinder in the software is straightforward since the 3D → Solids section already includes a preset cylindrical geometry. The Z-axis is designated as both the axial and third-dimensional axis.

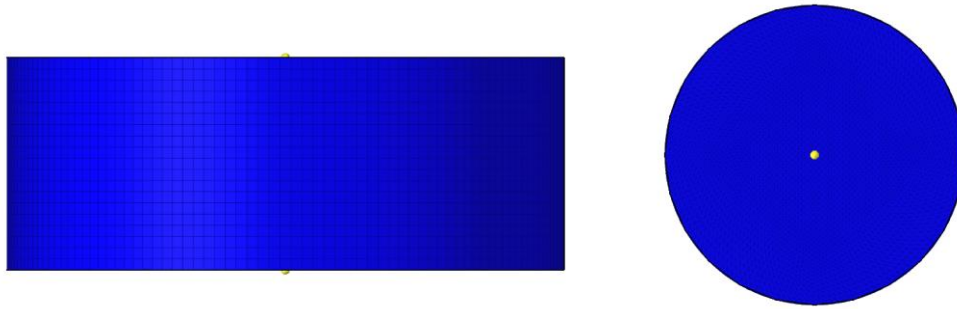


Figure 20: 3D sample model, top and side view

Once the cylinder is generated, the next step is meshing. Selecting the element type and size is critical, as they significantly impact the computational time and the simulation convergence. Ideally, the mesh should exhibit axial symmetry to avoid directional bias in deformation. In general, mesh density is a key parameter that affects both the accuracy of results, and the computational time required for the model. The model is composed by CPENTA elements, of 1x1 mm dimension, which are six-node pentahedral finite elements, the total number of elements is 1,225,552.

4.1.1 Constraints

For accurately simulating the consolidation shell, the correct setup of the constraints is essential. Since the ring allows only axial deformations, movements different from the axial one must be restricted. To accomplish this, create a "load collector," which serves to organize loads, constraints, and equations systematically.

In the Analyse → Constraints section, can be define the SPCs (relative single-point constraints). Here, most degrees of freedom (DOFs) in the model are limited. The base is restricted in the first three DOFs (x, y, and z), while the lateral surface is limited in the x and y directions only.

These configurations ensure that the model closely mirrors the actual physical behaviour of the tested material under consolidation conditions.

4.1.2 Material

The material used to model the soil is *loose sand*, and its behaviour is crucial for wheel contact, especially for off-road vehicles. Traction on loose sand is influenced by soil density, particle size distribution, wheel-ground pressure, and tread design. In geotechnical contexts, loose sand is studied for its properties of low cohesion, high compressibility, and low shear strength.

The Young's modulus E for loose sand may vary from a maximum of 35 MPa to a minimum of 10 MPa. For an initial iteration, the minimum value of 10 MPa is choose. The density was selected at a realistic value of $1.55e - 09$ tons/mm³ (1550 kg/m³).

The Poisson's ratio is set to 0.3. These initial values have been input into the *MATI* card. In the *MATSI* card, a work hardening value of $H=0$ was used to implement a perfectly plastic behaviour, with an initial yield point of 0.8 MPa (*Figure 21*). This yield point will be increased in subsequent iterations, but with no big differences, the solver is more sensitive to changes in the Young's modulus than to the yield point.

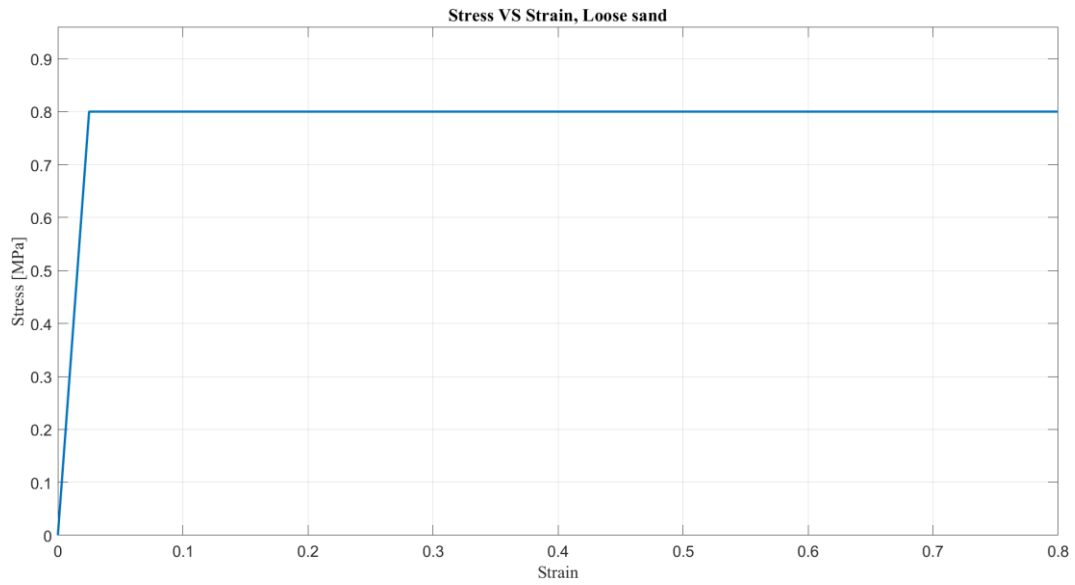


Figure 21: Loose sand characteristics

4.1.3 Load

The chosen type of simulation is a *non-linear transient analysis*. The axial load is computed from the available data of the normal stress known from the oedometer test (*Table 1*). Equation 13 describes the normal stress as function of the vertical force F and the area A :

$$\sigma = \frac{F}{A} \quad (13)$$

The values are presented in the following table (*Table 3*):

Table 4: Load values

F [N]
0
24.15
48.11
96.21
192.62
385.04
770.28
1540.36
3080.92
770.28
192.62
48.11
0

To apply this load uniformly to the upper surface of the sample, a rigid element RB is utilized. The RBE3 is a type of rigid element used in OptiStruct to distribute the load across a structure more realistically than RBE2 elements. Unlike RBE2, which creates a completely rigid connection between slave and master nodes by assigning infinite stiffness, the RBE3 does not have stiffness. Instead, it allows for the transfer of loads and displacements from the master node to the slave nodes without rigidly constraining them, making it suitable for load distribution rather than for creating a fully rigid connection.

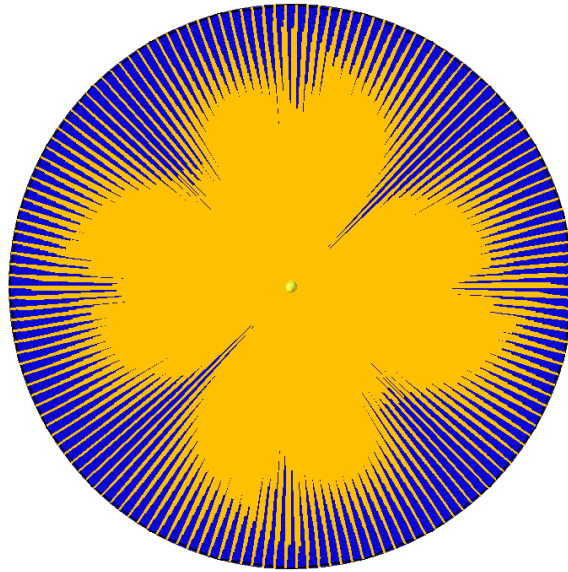


Figure 22: RBE3 element, top view

In conjunction with this, the *DAREA* card is used. In OptiStruct, the *DAREA* card is utilized to apply dynamic loads to specific degrees of freedom of the structure during dynamic analyses. It is often used in combination with other dynamic load cards, such as *TLOAD*. These cards enable us to specify the characteristics of the dynamic load in a *XY* plane. This setup allows for easy adjustments of the load specifications without the need to manually reset the specific position and intensity of the load each time.

The node specified in the *DAREA* card serves as the independent node of the RBE3 element. The location of the dynamic load application and the independent node significantly influences the simulation results. Initially, in the first iteration, the independent node was positioned at a generic height above the load application surface. However, based on the simulation results and the behaviour of the mesh, it became evident that this positioning could lead to undesirable mesh phenomena and generate unfavourable moments in the simulation. Therefore, it was decided to place the node coplanar with the upper surface of the sample.

The load was applied in steps over a total simulation time of 60 s (*Figure 23*).

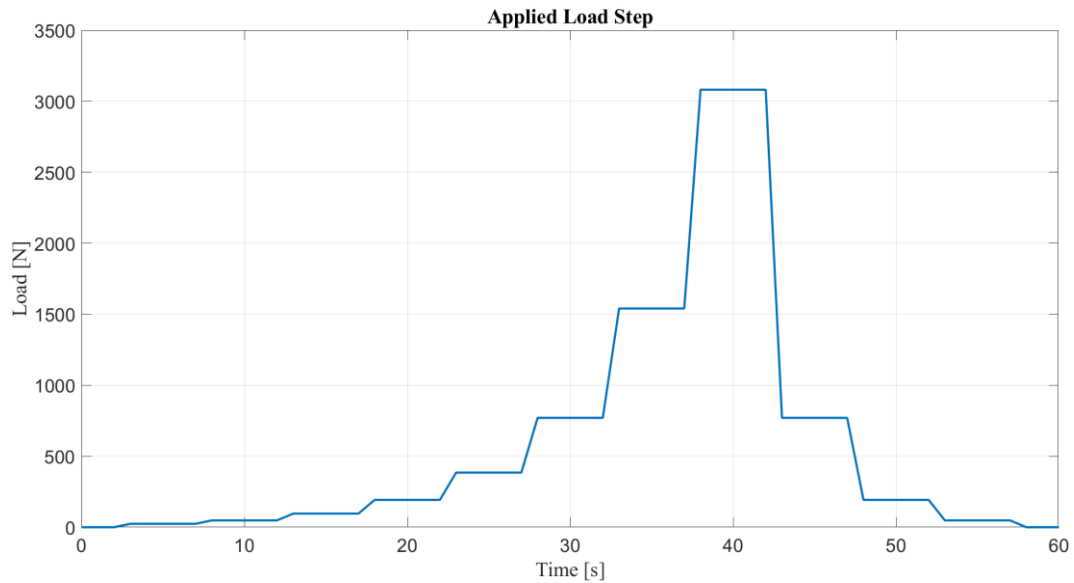


Figure 23: Load vs Time, curve for oedometer test

4.1.4 Time set up

A *TSTEP* card is required, which defines the time step parameters for control and specifies the intervals at which a solution will be generated and output in the transient analysis.

To create the *TSTEP* card in HyperMesh, first create a load collector, then in the type of card, specify *TSTEP*.

In this setup:

- N is defined as the number of time steps, each with a value of DT .
- DT represents the time increment for each step.

To simulate a total time of 60 seconds, select a value of $DT = 0.1$ seconds and set $N = 600$. This configuration ensures that the load is applied gradually, and the solver outputs results at consistent intervals across the entire simulation duration.

4.1.5 Results

For the tests, the oedometer test is used to understand how the program behaves and identify the parameters that influence the solver. First, match the experimental data within the material's elastic linear range, focusing on studying the Young's modulus and its behaviour within the model.

As discussed in Chapter 2, one of the fundamental graphs in this test is the consolidation curve (*Figure 9*), where it is studying the loading phase. In contrast to the oedometer test, in which the primary parameter of interest is the compression index, this analysis relies solely on Young's modulus as the adjustable variable. Varying Young's modulus and subsequently compare the compression index obtained from the tests with the experimental data, thereby ensuring that the material's behaviour aligns with the experimental results.

Soil mechanics typically refers to the void ratio, which is the ratio between the volume of voids (spaces not occupied by solid particles) and the volume of solid particles in soil or granular material. This parameter is fundamental for describing the relative density and degree of compaction of the soil, impacting its mechanical properties and permeability. In our case, considering the type of solver mentioned in Chapter 3, the particle component is not included in the model, as it can be studied using other models, such as DEM. Therefore, it's required a law that links the void ratio to strain.

The relationship between the void ratio e and strain ε can be simplified by considering that during compaction or dilation, the void ratio varies with the change in volume. The relationship is:

$$\varepsilon_v = \frac{\Delta e}{1 + e_0} \quad (14)$$

where:

- ε_v is the volumetric strain,
- $\Delta e = e - e_0$ represents the change in void ratio,

- e_0 is the initial void ratio.

This relationship indicates that the volumetric strain is directly proportional to the change in void ratio, normalized by the initial void ratio. Accordingly, in this case, a consolidation curve related to the strain ε rather than the void ratio is used.

Considering that only the linear section is being analysed, a linear-elastic perfectly-plastic behaviour has been selected for the tests. The solver is highly sensitive to this configuration because, if strains become excessive, the solver may encounter errors when it reaches the perfectly plastic section of the simulation. If necessary, a minimal amount of work hardening could be introduced in the material characteristics, specifically within the *MATSI* card as discussed in Chapter 3.

After setting up the simulation, an initial run was conducted with a Young's modulus value of 10 MPa and a linear-elastic behaviour.

Reviewing the consolidation curve, can be found that the results were not very close to the experimental data (*Figure 24*), though the Young's modulus remains within a realistic range of values.

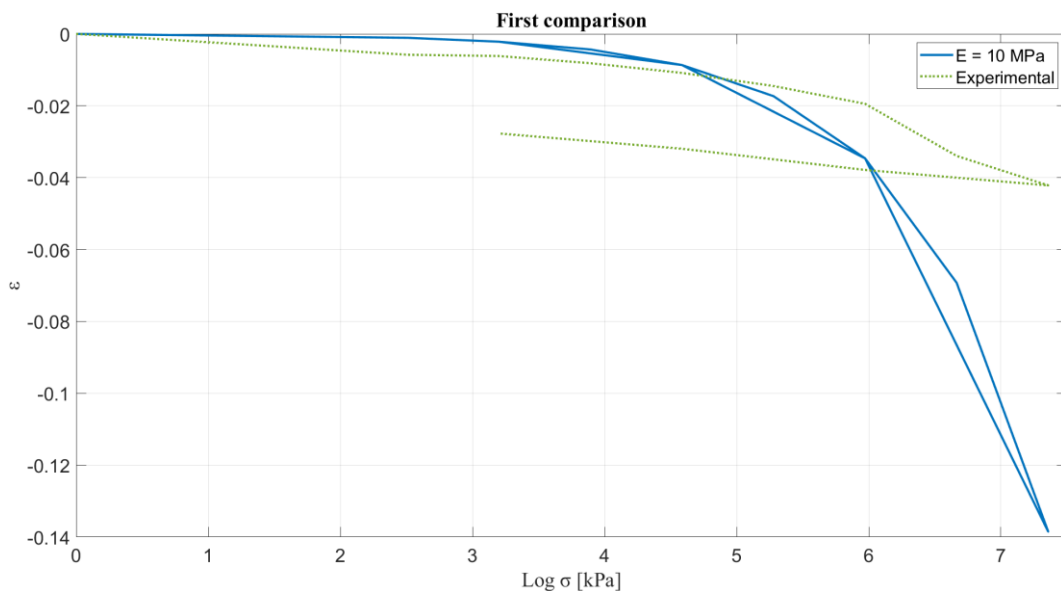


Figure 24: First comparison

To better understand the model's behaviour, a sensitivity analysis on Young's modulus is required (*Figure 25*). This will allow us to fine-tune the model

parameters, ensuring that the simulated behaviour more accurately reflects the real-world material characteristics. For the next step in the sensitivity analysis, also the material's perfectly plastic behaviour is considered.

Figure 25 compared the following simulations:

- Simulation considering a Young's modulus of 10 MPa with a linear elastic behaviour (blue curve);
- Simulations considering a Young's modulus of 32 MPa with two different yield point with a perfectly plastic behaviour (red and purple curves);
- The experimental data (green dotted curve).

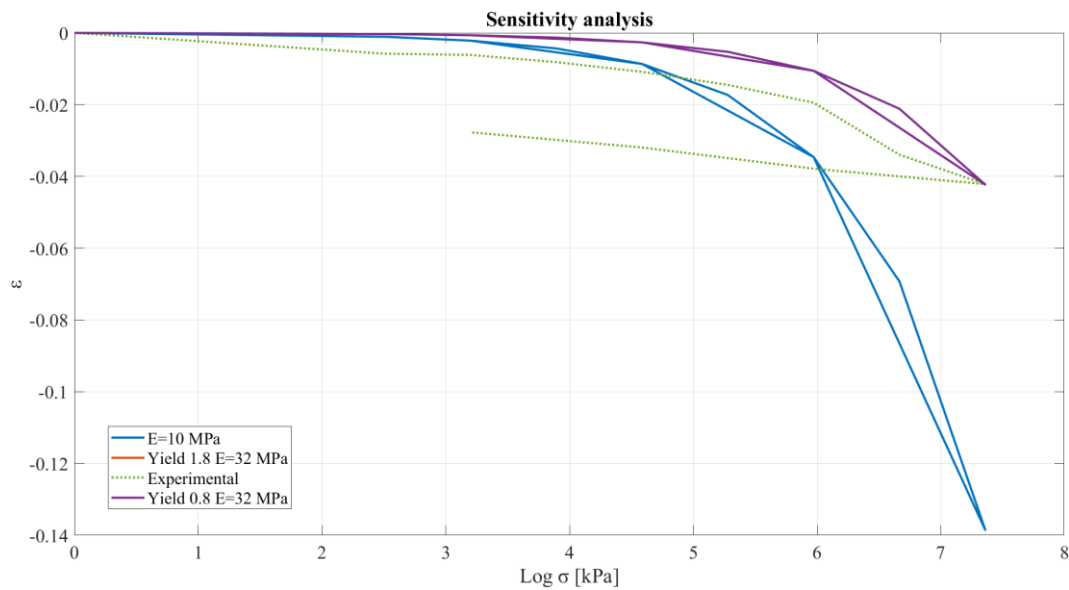


Figure 25: Sensitivity analysis

The sensitivity analysis demonstrates that the results are not affected by variations in the yield point. This confirms the assumptions of the oedometer test, where plasticity is not reached, as well as the simulation, which also does not reach the yield point; in fact, the two simulations at $E = 32$ MPa, despite different yield points (0.8 MPa and 1.8 MPa), yield nearly identical results. However, Young's modulus

does show a substantial influence on the data. The deformation at peak stress remains consistent across both cases.

The main difference between the experimental curve and the numerical curve is due to the exclusion of the reloading phase in the numerical analysis, as the related coefficient was not included in the model. Therefore, the numerical model only considers the normal consolidation curve. Examining the comparison with the experimental data, it is observed that the simulated curve does not closely align with the experimental results. Comparing the compression index, calculated using Equation 4 and focusing solely on the normal compression line, it can be observed that the value derived from the simulation remains higher than that of the experimental data (*Table 4*).

Table 5: Compression indices

	Cc
Experimental	-0.0164
E = 32 MPa	-0.0229

As shown, the simulated value is nearly double the experimental results. Since this type of test needs to consider the porous nature of soils (not available in the software), a Young's modulus of 32 MPa has been selected, and the focus has shifted to the triaxial test. The triaxial test is a more comprehensive method, enabling us to analyse a broader range of material properties due to its greater complexity compared to the oedometer test.

4.2 Triaxial test

In the FEM setup, a cylindrical soil sample is modelled with consolidation phase replicated through applying the confining pressure around its sides and top surface, while an axial deformation is increased vertically to replicate the shear phase of the laboratory test. The soil's response is defined by the Mohr-Coulomb constitutive

model, which characterizes yielding and plastic deformation based on cohesion and internal friction angle.

Precise boundary conditions and careful mesh refinement are essential to accurately represent stress-strain relationships, aligning the simulation closely with the physical triaxial test outcomes.

As is customary, the process begins with laboratory tests, which are then reproduced using finite element modelling. The first step involves defining the sample dimensions.

As discussed in Chapter 2, the sample of the experiments has diameter of 70 *mm*, resulting in a height of 140 *mm*.

Mesh selection is also essential in this case, as various mesh types were tested in a trial-and-error approach to determine the most suitable configuration. Initially, the model use CPENTA elements. CPENTA elements are often selected when a fully hexahedral (brick) mesh is challenging to implement, typically due to complex geometries that necessitate alternative meshing techniques. Pentahedral elements are useful in transitions or areas where hexahedral meshes may not fit easily, while still providing a more structured mesh compared to tetrahedral elements.

As shown in Figure 26, the resulting surface of the CPENTA-meshed sample lacks axial symmetry. Despite this, the chose of this configuration for the initial test stages, aiming to fine-tune the simulation setup effectively. This mesh configuration allow to gather essential data on parameter sensitivities and refine the model's boundary conditions and loading paths before transitioning to more sophisticated meshes.

The lack of axial symmetry tends to favour deformation in specific directions. This directional bias is partly a result of the denser mesh around certain points, which causes localized strain concentrations. However, the trial with CPENTA elements was critical to developing, setting up, and understanding the parameters necessary for an accurate triaxial test simulation. Upon completion of these initial stages, other mesh types will be explored to better capture axial symmetry and more

uniformly distributed deformations, which are essential for accurate triaxial modelling.

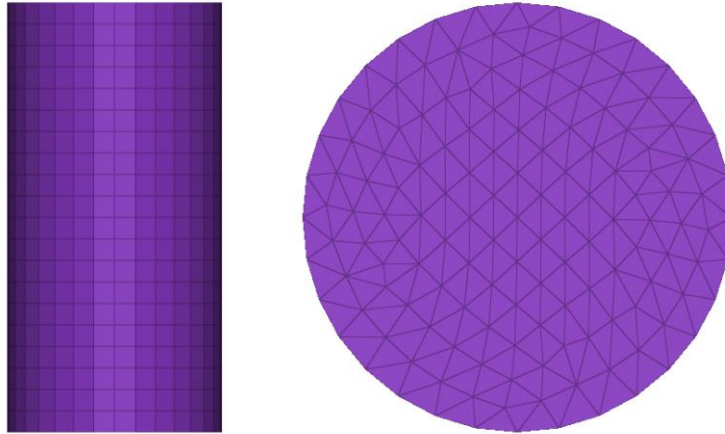


Figure 26: 3D sample model, top and side view

4.2.1 Constraints

In this case, the constraints are straightforward: constrain the bottom of the sample in the first three DOFs (x , y , and z), effectively fixing it at the base. As noted in Chapter 2, the physical sample is enclosed in a membrane. However, in this finite element model, do not include this membrane, as it is not considering the particle-based behaviour of the material, nor is there any fluid interaction.

The exclusion of the membrane and fluid in the model significantly simplifies the setup, as it eliminates the need to simulate the separation between the sample and the surrounding fluid medium. This approach focuses solely on the mechanical response of the soil sample under triaxial loading, streamlining the simulation while effectively capturing the essential stress-strain behaviour under investigation.

Isolating the sample from these additional complexities allows for more direct control and analysis of the impacts of load application, boundary conditions, and material properties on the core soil behaviour, without the influence of membrane interactions or fluid effects.

4.2.2 Material

As outlined at the end of Chapter 4.1, the process begins with data from the oedometer test, which was initially conducted to validate the elastic component of the model. For the first iteration, a linear elastic perfectly plastic material model is utilized, with parameters listed in the reference table (*Table 6*). The primary objective, however, is to implement the Mohr-Coulomb plasticity model, which more accurately represents the nonlinear behaviour of soils under stress.

Table 6: Material specification, loose sand, first iteration

MAT1		
E	32	MPa
NU	0.3	
RHO	1.55e-09	tonn/mm ³
MATS1		
TYPE	PLASTIC	
H	0	
YF	1 (Von Mises)	
LIMIT1	0,8	
TYPSTRN	0 Total strain is used on the x-axis	

The *MC* card in OptiStruct does not require the parameters specified in the *MATS1* card. Instead, the Mohr-Coulomb model independently calculates the material's yield and hardening characteristics based on the input parameters and the simulation conditions. This marks a significant difference: a yield criterion is applied (the Mohr-Coulomb failure envelope) rather than specifying a detailed material behaviour. For the second iteration, the MAT1 card parameters are combined with the Mohr-Coulomb (MC) parameters, with a specific focus on cohesion and the friction angle (*Table 7*).

Table 7: Definitive material card, loose sand

MAT1		
E	32	MPa
NU	0.3	
RHO	1.55e-09	tonn/mm ³
MATS1		
Mohr-Coulomb		
COHE	0	
FRICA	33	°
DILA	BLANK	

During testing, it can be observed that the *DILA* parameter, which represents dilatancy material response. Although *DILA* theoretically accounts for dilatancy effects, setting it to zero ($DILA = 0$) leads to excessive softening in the material, diverging from expected results. As first attempt, the value of *DILA* is set equal to the friction angle. This configuration aligns closely with the experimental data, as it provides a more balanced representation of the material's strength and deformation characteristics, allowing the model to replicate realistic soil behaviour under triaxial loading conditions.

This refined approach with the Mohr-Coulomb parameters significantly enhances the model's ability to approximate the observed experimental stress-strain behaviour, providing a more accurate foundation for further simulations and analysis.

4.2.3 Load and Enforce displacement

To simulate the consolidation phase of the specimen and to observe how the shear strength varies under different consolidation pressures, the effect of confining pressure is modelled, as discussed in Chapter 2. In laboratory tests, the shear strength of the soil increases with confining pressure. A constant pressure is applied to the lateral and upper surfaces, with the bottom face fixed to represent the base support (consolidation pressure).

This constant pressure acts orthogonally to the mesh surfaces, simulating the effect of an enclosing membrane without the complexity of fluid-structure interaction. To implement this pressure load, a similar approach previously presented in Chapter 4.1 is used. However, in this case, the *DAREA* card is not used. Instead, a pressure is applied directly to the surfaces using a load collector with the *PLOAD4* card, which allow the application of the pressure on 3D element faces.

To manage the temporal progression of the pressure, the *PLOAD4* card to a *TLOAD* card are used together. This setup allows for the control of pressure application over time, with an XY plot used to define the pressure curve during the consolidation phase. This confining pressure simulates the real consolidation process, where the specimen is pre-stressed before shear loading begins.

This method provides flexibility in adjusting the magnitude and distribution of confining pressure across different simulation stages

The test is repeated three times using three different levels of confining pressure, as listed in the Table 8.

Table 8: Confining pressure

Confining pressure [MPa]
0.05
0.2
0.8

Once configured, the confining pressure is set to be applied immediately from the start and to remain constant throughout the entire duration of the test.

Next, the stress-controlled approach is adopted for applying the load (shear phase). Here, the load is imposed dynamically, offering the advantage of easily adjusting testing conditions as needed. A similar setup to the one employed in the oedometer test was used, incorporating a rigid RB3 element along with the *DAREA* card to apply the target stress. Given the known confining pressure and desired effective stress on the sample's surface (as specified in *Table 2*), the applied axial load was adjusted to achieve these conditions.

To control the load application over time, *TLOAD* card is used. This approach mirrors the real test conditions, where the load is applied incrementally in stages, enabling the gradual increase in stress experienced by the specimen during the physical test.

To apply both types of dynamic loads simultaneously, a specialized card called Dynamic Load Combination is used, which allows the combination and scaling of multiple dynamic loads within a single simulation. For this card to function effectively, a default scaling factor needs to be set, which in this case is set to 1, as there is no need to amplify or reduce the previously defined dynamic loads (*DLOAD*). This scaling factor ensures that each load is applied at its original intensity.

Under the scaling parameter, the number of *DLOAD* entries to be combined is specified, and a weight is assigned to each load. To match the original profiles specified in the *TLOAD* cards, a scaling factor of 1 is assigned to both loads, ensuring that they act as intended without modification to their intensity or behaviour.

After configuring the dynamic load combination, the simulation setup is finalized.

However, during preliminary simulations, the model encountered convergence issues with both the perfectly plastic material model and the Mohr-Coulomb plasticity criterion. The simulation consistently failed with the error message "Minimum time increment reached". Based on the help documentation, one

possible solution was to increase the *NINC* parameter, which defines the number of implicit load sub-increments, to provide finer control over the load application and improve stability or to move to a different excitation, in this case an enforced displacement.

It was observed that under high loading conditions, the mesh exhibited abnormal deformations, resulting in excessive strain levels and eventual non-convergence. This issue likely stems from the perfectly plastic behaviour of the material, where the absence of strain hardening causes uncontrolled plastic deformation as the stress increases. As the load approaches the material's yield limit, the high degree of plasticity results in localized deformations that the mesh cannot support (*Figure 27*), ultimately destabilizing the model.

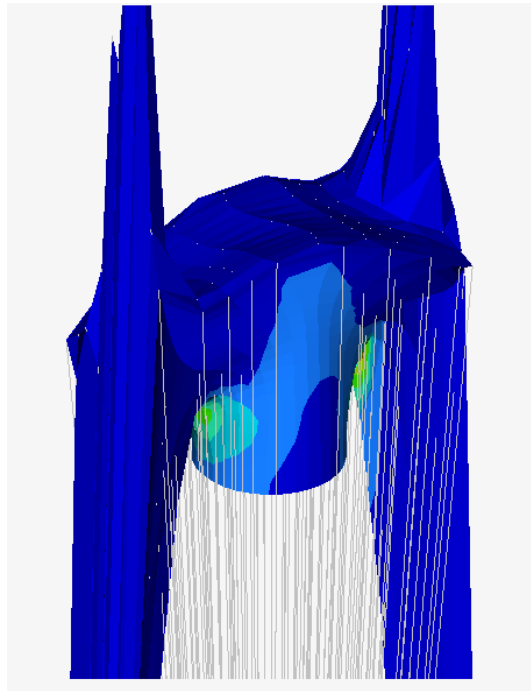


Figure 27: Mesh excessive deformation

After obtaining the results from the stress-controlled method, the strain-controlled approach was tested. In this method, a controlled deformation is applied to the top surface of the sample by enforcing a specific displacement, rather than applying a direct force as the load input.

For the initial test, only an RB2 element was used, with a displacement set at 10% of the specimen's height, equivalent to approximately 14 mm. This displacement level was chosen to introduce a significant deformation while remaining within realistic test limits, due to the fact that usually the test is stopped when it's reached the 20% of axial deformation.

To impose an enforced displacement, a similar procedure to that used with the *DAREA* card for force application is used. However, in this case, the *SPCD* card is utilized, this card allows to define an enforced displacement, velocity, or acceleration for dynamic analysis. The *SPCD* card enables the direct control the deformation applied to the model, specifying exact displacement values at the nodes of the upper surface.

Once again, the *TLOAD* card is used to manage the displacement dynamically over time.

Despite completing the simulation, the results were unsatisfactory. The mesh exhibited unusual deformations, with irregular strain distributions and unrealistic displacements. This abnormal behaviour suggests that the mesh configuration or boundary conditions may need adjustment to handle the large deformation more effectively. Possible causes include issues with element distortion due to excessive displacement, as well as potential limitations in the element formulation for handling strain-controlled conditions under large displacements.

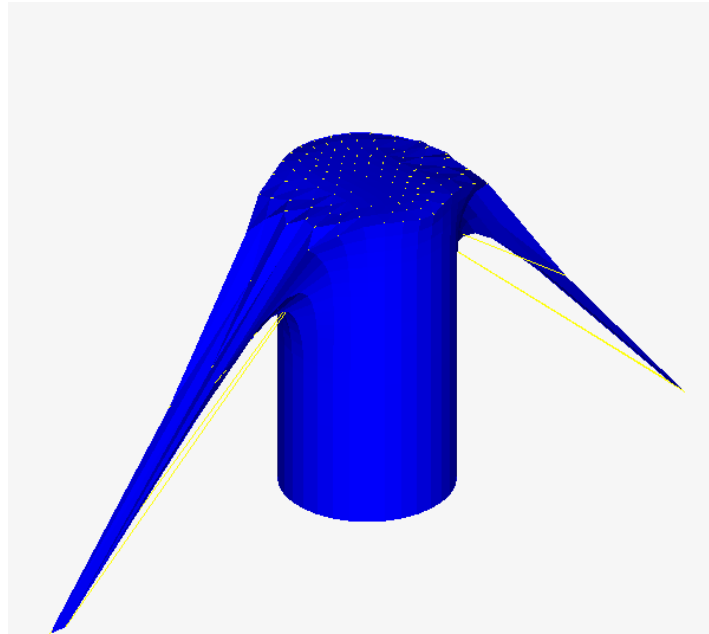


Figure 28: RB2 enforced displacement

These findings highlight the need for further refinement of the model. To address this issue, a rigid plate is used, it moves vertically downward onto the top surface of the sample to apply the desired deformation. This infinitely rigid plate, whose dimension are listed in the table 9, ensures that displacement is uniformly transmitted across the specimen surface.

Table 9: plate dimension

AREA	80x100	mm
ELEMENT DIMENSION	5x5	mm
ELEMENT TYPE	QUAD	

In OptiStruct, interactions between solids or between solids and surfaces require defining a contact. The HyperMesh preprocessor provides an auto contact function, which automatically identifies potential contact pairs based on a specified search distance and contact type. By identifying the two components, setting the contact search distance, and specifying the contact type, it enables the realistic interaction between the rigid plate and the sample.

For this case, a *sliding* contact type is selected, which provides only normal contact stiffness at the contact interface without accounting for frictional effects. HyperMesh allows for the selection of multiple contact types and the direct specification of static and dynamic friction coefficients if needed. However, for this setup, friction was excluded to simplify the contact conditions.

Initially, all simulations using the rigid plate failed when a perfectly plastic behaviour, with convergence issues persisting. These observations suggest that introducing strain-hardening parameters would improve the simulation's stability and better reflect realistic soil behaviour under progressive loading conditions.

This hypothesis was confirmed through simulation: the model responded positively to the revised setup. As seen in prior tests, the purely perfectly plastic behaviour resulted in high levels of plasticity that prevented convergence, underscoring the need for strain-hardening in order to achieve stable and realistic results. This refined approach provides a more reliable simulation of soil deformation under controlled strain, effectively balancing load application and material response.

The only issue with this simulation was that the specimen partially penetrated the plate during loading (*Figure 29*). To resolve this problem, the dimensions of the plate is increased. It is recommended that the plate's dimensions be set to 2-3 times the smallest upper surface diameter of the sample. The updated plate dimensions, shown in the table 10, effectively eliminate the mesh overlap, preventing any unintended penetration.

Table 10: New plate dimension

AREA	200x200	mm
ELEMENT DIMENSION	5x5	mm

With these revised plate dimensions, the interaction between the plate and the specimen mesh is stable, ensuring consistent contact without mesh interference throughout the simulation.

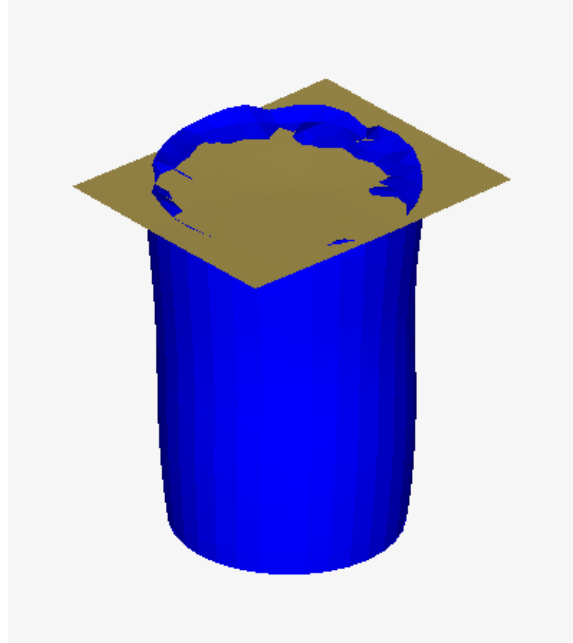


Figure 29: Mesh interference

In the latest iteration, the type of mesh was changed to achieve greater axial symmetry and avoid the localized deformation phenomena observed previously. Hexahedral elements, each with 8 nodes, were used. The elements have a size of 5x5 mm, with 44 elements along the circumference and 28 elements along the height. This mesh refinement (*Figure 30*) aims to improve the overall structural behavior and reduce the risk of anomalous deformations during the analysis. In combination with the increased plate dimension.

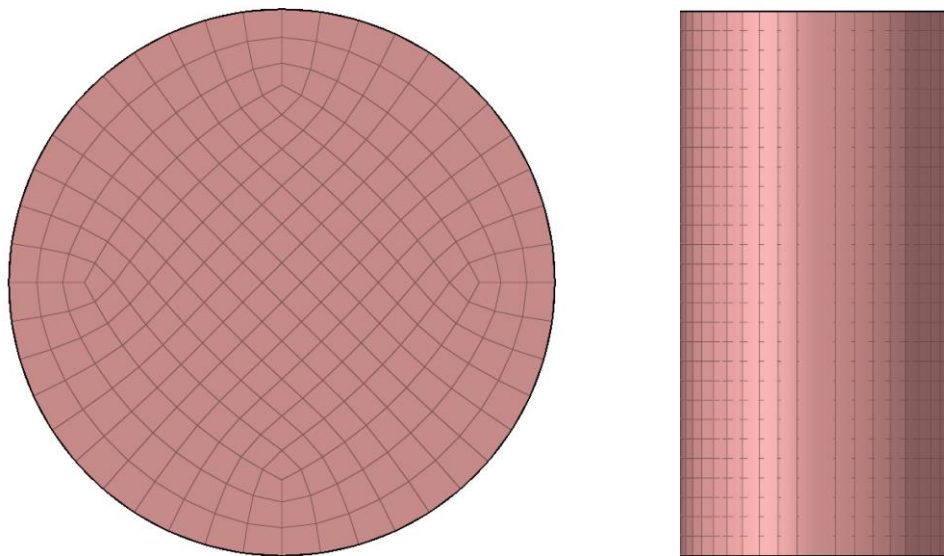


Figure 30: Last iteration model

4.2.4 Time set up

The duration of this test typically spans several hours or even days under real conditions. However, with this simulation tool, the testing time can be significantly reduced. For this simulation, the total time is set to 10 minutes, allowing the enforced displacement to be applied over that period. Given a target deformation of 15% (or 21 mm), this results in a strain rate of approximately 0.035 mm/s.

To achieve this, a time increment DT of 0.1 seconds and set $N = 6000$ steps is defined, providing a total simulation duration of 600 seconds (10 minutes). This setup balances computational efficiency and accuracy, allowing us to replicate the deformation behaviour in a fraction of the time required for physical testing.

4.2.5 Results

After extensive testing, the Mohr-Coulomb criterion was successfully implemented. The simulation now consistently converges, and as explained in

Chapter 3, simulations driven by enforced displacement typically converge more readily.

In the *Material* section of this chapter, the Mohr-Coulomb implementation is outlined, with parameters listed in Table 7. All three simulations with varying confining pressures achieved successful convergence, allowing for the analysis of the experimental data to proceed. The comparison of the stress-strain curves from the tests with those from the experimental data was performed.

In our simulations, two distinct phases were observed. As discussed in Chapter 3, the model does not simulate the saturation phase; instead, it proceeds directly to the consolidation and failure phases. Additionally, stress-strain curves do focus on the shear phase (*Figure 31*). The stress-strain curves are constructed by using displacement and stress data, considering only the deformations starting from the onset of shear phase. To calculate axial strain, the initial height h_0 is defined as the initial specimen height (140 mm) minus the displacement Δh due to consolidation. Then the strain is evaluated through the relation $\varepsilon = \frac{\Delta h}{h_0}$.

The graph reveals that the elastic linear phase in the simulation lacks the hardening effect observed in the experimental curves (*Figure 31*). This discrepancy likely stems from the solver and the specific characteristics of the material and test setup.

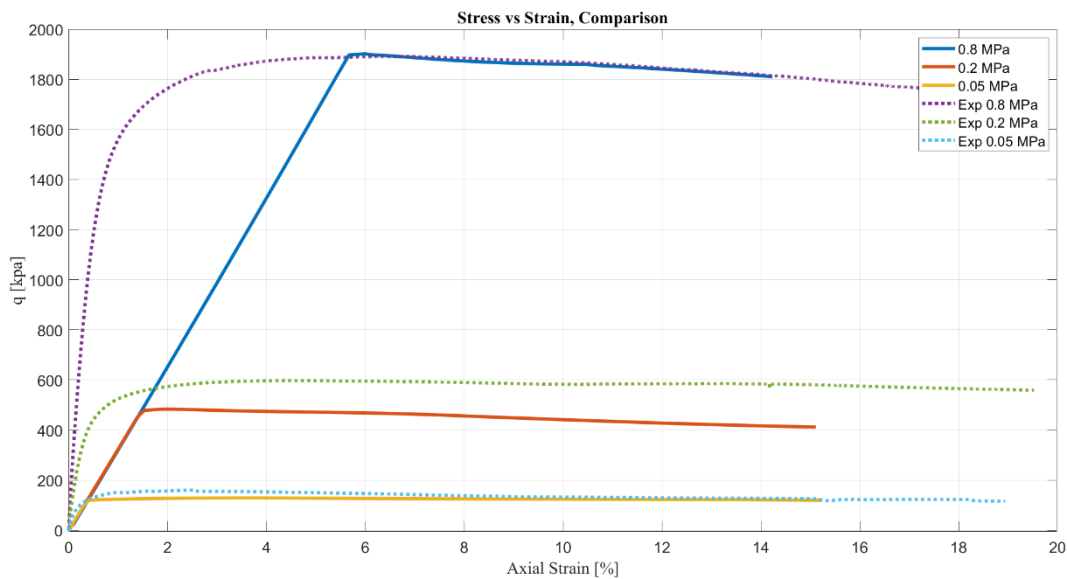


Figure 31: Comparison, Experimental data with Simulation data

Additionally, our tests indicate that the solver is highly sensitive to the Young's modulus, as expected and described in Section 4.1. An increase in Young's modulus results in a steeper elastic portion of the curve, while a lower modulus produces a gentler slope. In the simulations using the Mohr-Coulomb criterion, it was further observed that a lower Young's modulus delays the peak failure point, and required a lower stress level to reach it.

This behaviour can be observed by conducting a sensitivity analysis, holding the consolidation pressure constant and varying the Young's modulus. In figure 30, this previously discussed behaviour is illustrated. In this case, the sensitivity analysis was performed with a consolidation pressure of 0.05 MPa.

The figure 32 shows that the curve with $E = 32$ MPa reaches a higher peak value compared to the curve with a lower Young's modulus.

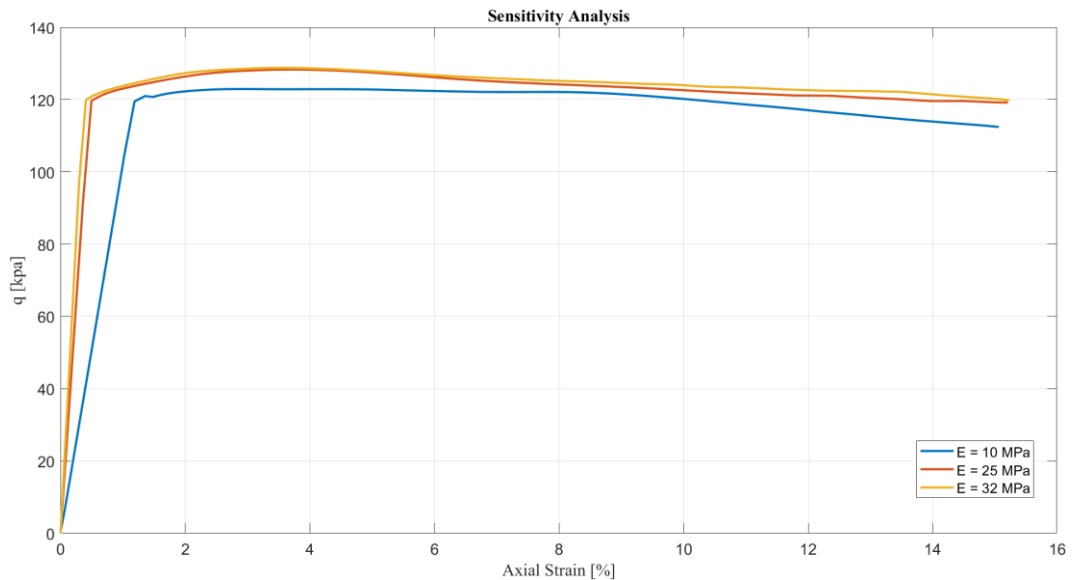


Figure 32: Sensitivity Analysis, $\sigma_c = 0.05$ MPa

When analysing the stress-strain curves more closely (Figure 32), the peak values in the simulation align closely with the experimental data, especially for the curves

with confining pressures of 0.05 MPa and 0.8 MPa. However, for the 0.2 MPa confinement curve, the simulated values are lower than the experimental results. This divergence suggests a notable difference between the numerical model and the material's physical behaviour. Examining this difference provides a better understanding of the model's behaviour and its divergence from the experimental data.

Acquiring the data of the peak stress obtained from the simulations, allows for construction of the critical state line. This line provides valuable insights into the model's correct functioning and offers data to validate the parameters ϕ and c that have been set.

Analysing this critical state line allows us to assess whether the model behaves as expected under different conditions, confirming if the chosen parameter values align with theoretical predictions and experimental trends.

The values of ϕ and c set for the simulation produce peak values for the three simulations, each with different confining pressures, that align directly along a straight line. (*Figure 33*).

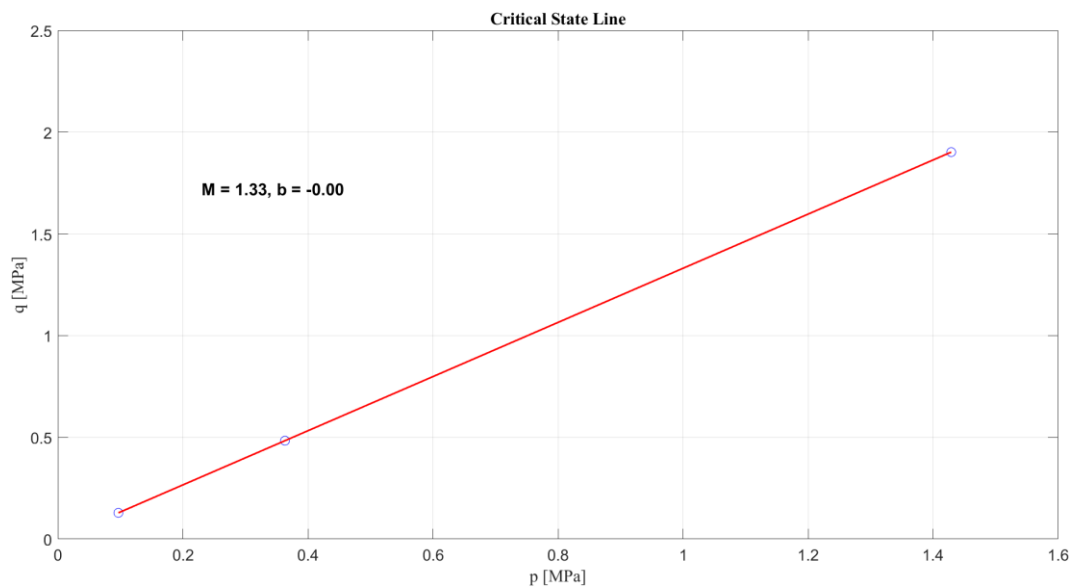


Figure 33: Critical State Line of the model

In contrast, an examination of the experimental data reveals that the peak at 0.2 MPa does not align with the interpolating line. This discrepancy arises because, in real-world conditions, the line is interpolated between the three peak points measured during the three tests. Consequently, the experimental curve at 0.2 MPa appears higher than the simulated curve. This behaviour can be explained by the fact that the line serves as an interpolation, so it is not expected that all points will coincide perfectly with it, in figure 34 black circles correspond to the experimental value, instead the blue one to the simulation. In contrast, in the numerical model, the values are expected to align, as the exact behaviour the model should follow is explicitly defined.

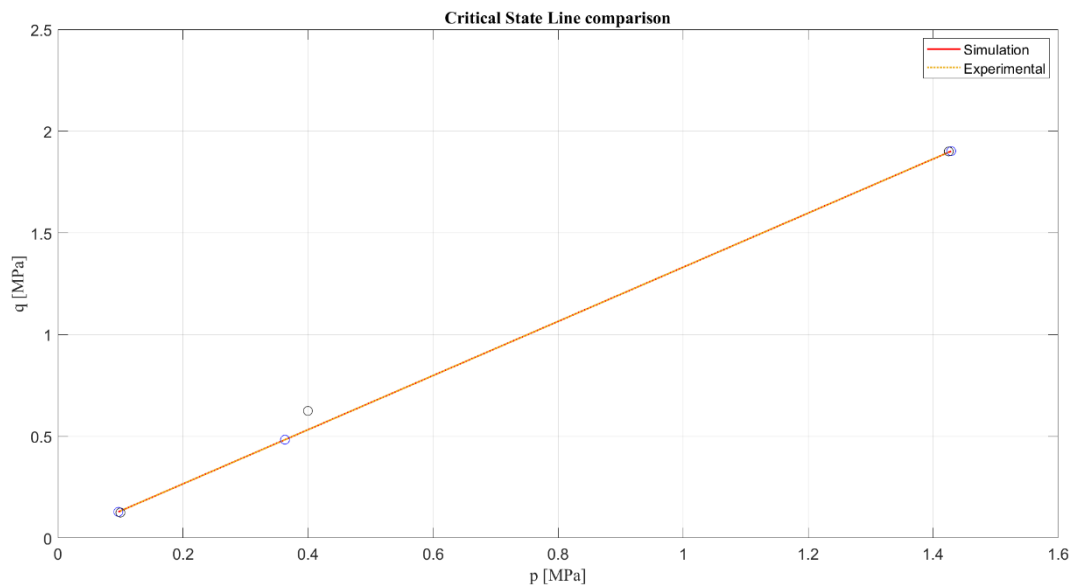


Figure 35: Comparison Critical State Line

A further verification of the correct functioning of the criterion can be obtained by calculating the values of ϕ and c from the Critical State Line (CSL) constructed through the simulations. Following the procedure outlined in Chapter 2.

First, the slope of the line (m) is obtained, which is 1.33. Using equation 8, the value of ϕ is evaluated, which is 32.99° .

Next, with ϕ known, the active earth pressure coefficient is calculated using equation 10. Finally, knowing the intercept of the Critical State Line and the active

earth pressure coefficient, c is defined using equation 9. The result of this calculation is $c = 0.00001$.

These values show that the calculations are consistent with those set in the model.

After verifying the numerical functionality of the model, attention is focused on visualizing the specimen and analysing its behaviour as it approaches the peak stress condition. The two states of the specimen: the undisturbed initial state and the peak stress condition.

Observing the mesh behaviour, it can be note that no signs of localized deformation are present up to the peak stress. Instead, the specimen undergoes a uniform deformation, gradually taking on a barrel shape, consistent with expected behaviour in real-world conditions under similar stress. This uniform deformation reflects the anticipated response of the material, confirming that the model effectively simulates the specimen's behaviour up to the peak stress without artificial localization effects.

4.3 Pressure-Sinkage test

This section of the chapter addresses the study conducted for the development of the pressure-sinkage test.

The analysis begins with the data obtained from the triaxial test to define the material properties that will serve as the foundation for the simulations. Specifically, a Young's modulus (E) of 32 MPa is selected, as this value is deemed the most appropriate based on the calibration. This selection is based on the peak value only, without considering post-peak behavior.

Given the known material parameters, the aim of our study is to observe how the solver operates and how the soil model behaves under two primary load application scenarios. These scenarios include:

1. Direct application of load on the surface of the soil model.

2. Interaction between a plate and the soil, where the load is applied to the plate.

To implement the tests, a cubic soil domain is modelled with the following specifications:

Table 11: Sample dimension

DIMENSION	400x400x400	mm
ELEMENT TYPE	HEXA	
ELEMENT DIMENSION	10x10	mm

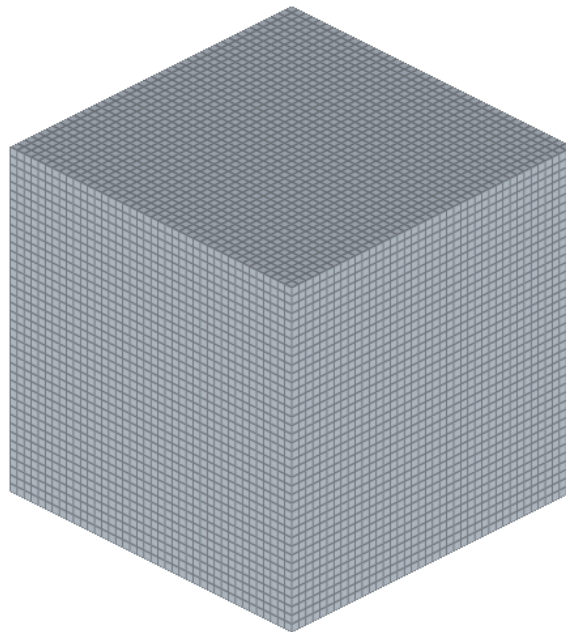


Figure 37: Cubic soil model

The material properties used in the simulations are as follows:

Table 12: Material card, loose sand

MAT1		
E	32	MPa
NU	0.3	
RHO	1.55e-09	tonn/mm ³
MATS1		
TYPE	PLASTIC	
H	0.5	
YF	1 (Von Mises)	
LIMIT1	0,8	MPa
TYPSTRN	0 Total strain is used on the x-axis	

The load application for both tests was chosen to be very slow, simulating a quasi-static loading condition. A uniform load of 0.2 MPa will be applied over a circular area with a radius of 50 mm. In the case of the plate-soil interaction, the plate dimensions will match the circular load area.

4.3.1 Boussinesq

To analyze the behavior of the model and the distribution of stresses within the soil, the Boussinesq method is considered. This method, through specific assumptions, allows for the determination of the stress state within the soil, given a known applied load and the geometry of its distribution.

The Boussinesq method is based on some assumption: the soil is treated as an elastic, semi-infinite, homogeneous, and isotropic solid. This approach is commonly used to calculate the increase in stress caused by foundation loads. It makes possible to determine how an applied load is distributed into the subsurface, generating a "stress bulb" that propagates from the point of load application and extends deeper into the ground, as depicted in the reference figure (*Figure 38*).

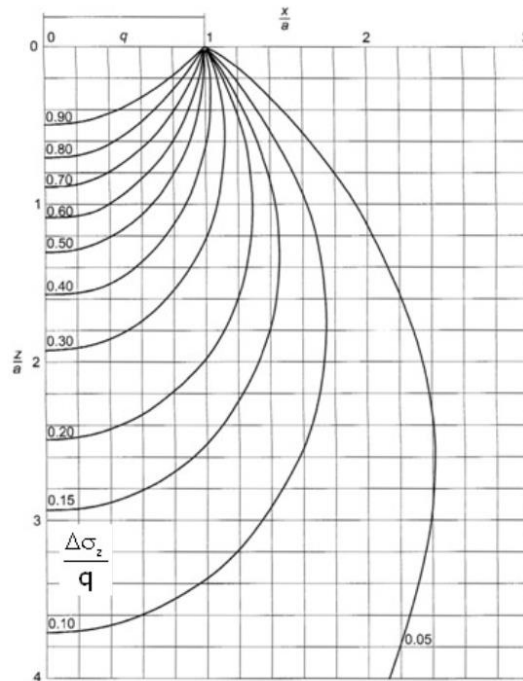


Figure 38: Stress Bulb for circular area. In the axis, horizontal and vertical positions of each considered point are normalized with respect to the dimensions of the plate.

It is important to note that the Boussinesq method assumes that the applied load must be a fraction of the critical load, since the main hypothesis is to lie into the elastic domain of the soil behavior. Although the assumptions inherent in this method lead to a degree of approximation, the precision achieved is generally considered acceptable for most practical applications, such as foundation design analysis.

The reference figure (*Figure 38*) illustrates the stress increments induced by a load q applied on a circular surface of radius r , providing a useful representation for understanding the distribution and evolution of stresses within the subsurface.

To reproduce the test conditions, a load of 0.2 MPa is applied on the soil surface using a circular geometry with a radius of 50 mm. This allows us to refer to the Boussinesq chart, specifically designed for load applications with circular geometry. By analyzing the simulation results, it can be observed that the model's behavior exactly matches the predictions made by the Boussinesq method.

Specifically, at the point of load application, the stress value is equal to the applied value of 0.2 MPa (Figure 39), confirming the correct initial distribution of the load.

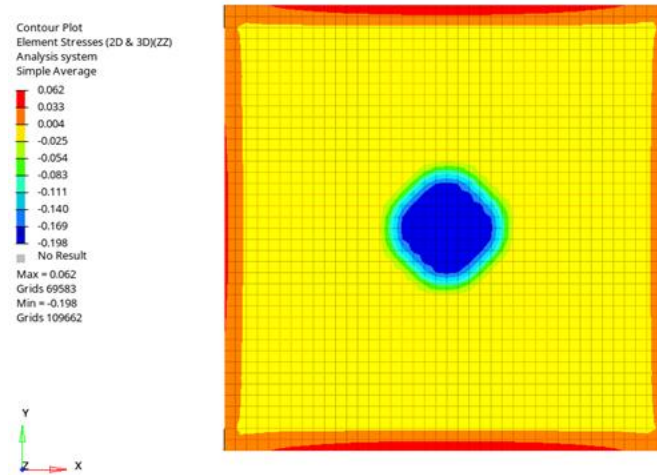


Figure 39: Sample Top view, axial stress

The figure 40 illustrates a stress distribution resembling the characteristic "stress bulb" described by Boussinesq, which propagates beneath the ground from the load application point. To further verify the accuracy of the model, a reference depth of 80 mm is selected below the surface for analysis.

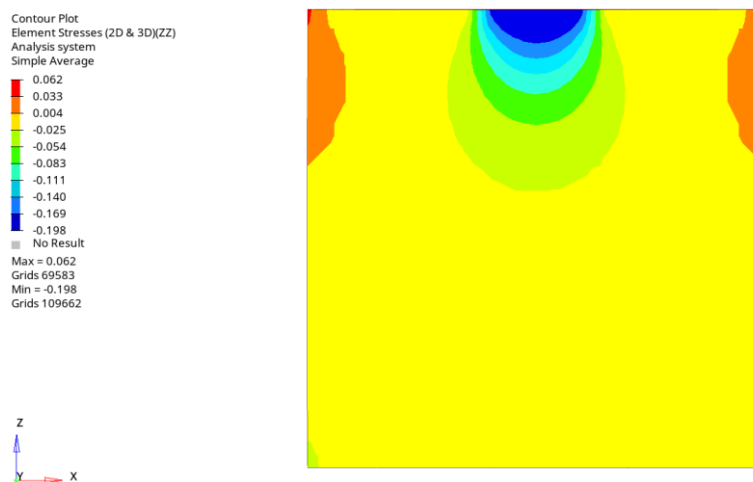


Figure 40: Cut view, Stress distribution

Using the Boussinesq chart, the depth is normalized relative to the radius of the applied load geometry through the ratio z/r . For this case, with $z = 80$ mm and $r = 50$ mm, the ratio is 1.6. By entering this value into the chart, the corresponding isocurve at 0.4 is identified.

With this known value, the relationship $\Delta\sigma/q = 0.4$ can be determined. Consequently, the stress value at a depth of 80 mm, calculated as $\Delta\sigma = q \times 0.4$, results in 0.08 MPa. Upon analyzing the simulation, it is found that the axial stress measured at a depth of 80 mm matches this theoretical value precisely, confirming the accuracy of the simulated model.

4.3.2 Plate version

For the next test, the contact between an infinitely rigid circular plate and the soil is considered (*Figure 41*). The experiment will be similar to the previous one, but in this case, the load will be applied to the plate. This configuration falls within the scope of geotechnical problems involving soil-structure interaction, particularly for foundation structures. The plate has the characteristics showed in the table below:

Table 13: Plate specification

PLATE RADIUS	50	mm
ELEMENT DIMENSION	5x5	mm
ELEMENT TYPE	QUAD	

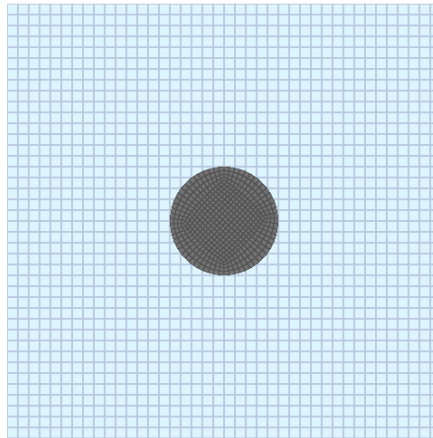


Figure 41: Top view, test model

In the initial tests, it was observed that in this configuration, load transmission is not immediate. By analyzing the stress state beneath the plate, it is evident that the recorded stress value is lower than the applied 0.2 MPa. This behavior is mainly due to contact stiffness. Specifically, OptiStruct uses nonlinear contact formulations, such as the Penalty method, to solve contact problems. These methods apply reaction forces only when the contact surfaces slightly overlap, which can reduce force transmission compared to a fully rigid contact. In a Penalty formulation, the contact force is proportional to the penetration of the surfaces. Increasing the contact stiffness in the model reduces the penetration and increases the reaction force, while lower contact stiffness results in less force transmission.

At this stage of the study, the focus was initially on verifying load transmissibility and subsequently on the stress distribution within the model.

The stick condition was applied between the two surfaces to prevent relative slipping, aiming to achieve the most rigid contact possible. Furthermore, the specific contact card is modified to define the stiffness value. The *PCONT* card allows specifying the type of contact between surfaces and adjusting different contact parameters. Regarding contact stiffness, it is possible to select different preset values:

- *AUTO*

- *HARD*
- *SOFT*

It is also possible to define specific values, expressed in $[N/mm]$. In the initial tests, the differences between the *SOFT* and *HARD* presets were examined. It was observed that the *HARD* preset provides greater load transmissibility compared to *SOFT*, though the measured stress value remained below 0.2 MPa. With the *HARD* preset, a value of 0.168 MPa is recorded, representing a 16% reduction in the applied stress.

Since no precise value for contact stiffness was specified, further tests were conducted to identify the most suitable value to achieve good load transmissibility, allowing for comparison with the previous test without the plate. Starting from very low values, such as 10 N/mm, it was determined that a value of 1000 N/mm provided excellent load transmissibility. In this case, the maximum recorded stress value was 0.197 MPa. Additional tests may help identify a possible threshold for result variation or a convergence limit for the model.

Given this behavior, similar occurrences can be expected in other types of contacts, which should be considered during the model design phase.

With this configuration, the analysis of the stress distribution can proceed. The goal is to achieve maximum load transmission to verify whether the Boussinesq method even with the presence of the contact plate or if the stress distribution changes.

The problem being addressed involves the behavior of a rigid footing on deformable soil, as illustrated in figure 42.

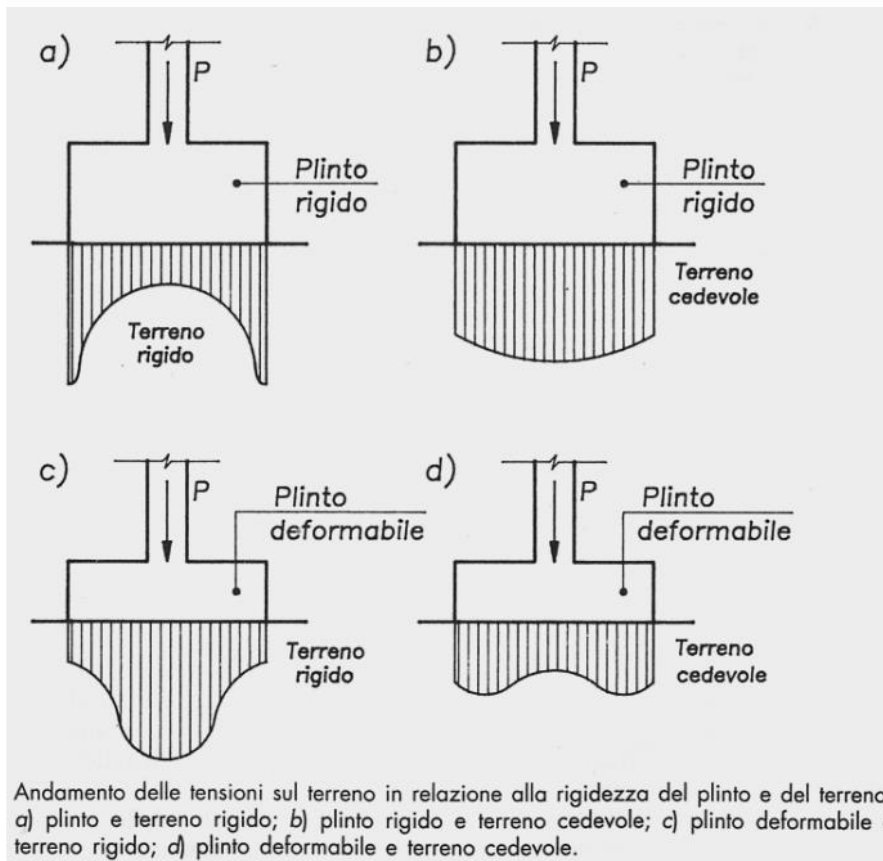


Figure 42: Stress behaviour for different configuration

The footing is a crucial element of foundations, designed to distribute the building's load over a larger surface area, thus reducing the pressure exerted on the underlying soil. This concept is fundamental not only in structural engineering but also in geotechnical studies, where it is assessed whether the footing correctly distributes loads based on the soil's properties, such as strength and bearing capacity.

The first objective was to reproduce an infinitely rigid plate on the deformable soil. Therefore, an analogous distribution to that observed by directly applying the pressure in the top surface of the model is aimed.

From the observed stress distribution, it is noted that, the maximum stress value occurs at the periphery of the plate, with a magnitude of 0.197 MPa, while the central area displays a lower stress value (Figure 43). This contrasts with what would be expected, namely, a maximum stress value in the central region of the footing. Attempts are needed, through acting on the contact stiffness of the contact

soil-plate and the plate itself, to perform a sensitivity analysis of the problem, and reach a more uniformly distributed soil pressure at the contact.

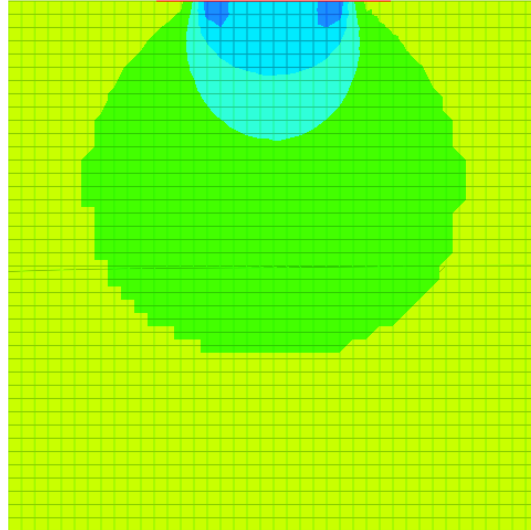


Figure 43: Cut view, Plate configuration, Stress distribution

A more specialized solver for yielding soils would likely offer parameters that allow for a more accurate representation of this behavior.

4.3.3 Pressure sinkage model development

This section describes the study conducted for the implementation of the pressure-sinkage test, aimed at determining terrain bearing capability. The approach followed is initially based on simplified test conditions, adopted for a preliminary iteration of the model.

A soil cube was generated and made to interact with a circular plate assumed to be infinitely rigid. Using the 3D section of the preprocessor, the cubic geometry of the soil was defined. Subsequently, to create the circular plate, a circular line was generated through the *topology* section of the software. The line was then extended into a surface using the 2D section.

The parameters related to the two components are presented in the table below:

Table 14: First iteration specification

SOIL MESH	11x11	mm
PLATE MESH	9x9	mm
SOIL DIMENSION	500x500x500	mm
PLATE RADIUS	75	mm
PLATE THICKNESS	2	mm
TYPE ELEMENT SOIL	HEXA	
TYPE ELEMENT PLATE	QUAD	

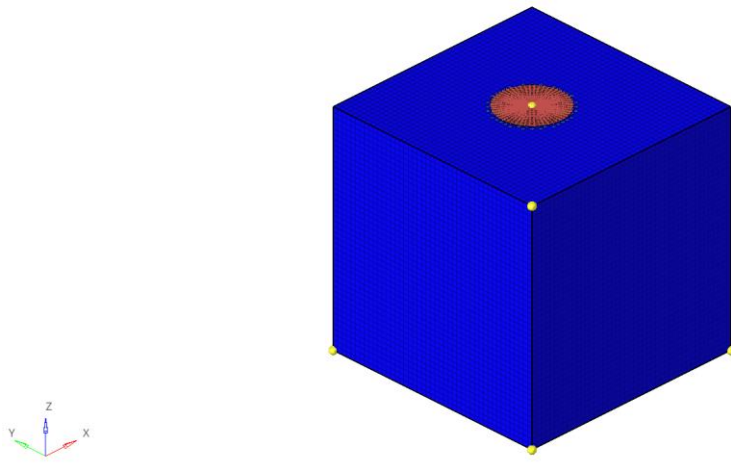


Figure 44: First iteration model

For the material properties, a linear elastic perfectly plastic behaviour was initially selected, using the characteristics of a clayey soil derived from a similar study (Ragheb, El-Gindy, & Kishawy, 2013).

Table 15: Material characteristics (Ragheb, El-Gindy, & Kishawy, 2013)

Soil Type	Elastic Modulus, E (MPa)	Bulk Modulus, K (MPa)	Shear Modulus, G (MPa)	Yield Stress, Y (MPa)	Density, ρ (ton/mm ³)
Clayey Soil	24	15	9	0.016	1.60E-09

In this case, constraints were applied exclusively to the base of the cube, restricting only the first three degrees of freedom.

An enforced displacement of 10 mm was then applied using the *SPCD* card, following the same procedure as in the triaxial test described earlier in this chapter.

This initial model was tested with various contact configurations. First, the slide contact is tested, which does not account for friction between the two surfaces. With this setting, the simulation easily achieved convergence. Subsequently, a static friction contact was defined using the *PCONT* card. In this scenario, the simulation failed because the solver detected excessively high friction levels and was unable to achieve convergence.

Finally, as a last test, a combination of static and dynamic friction coefficients is considered.

The corresponding values are shown in the table below:

Table 16: Friction specification

STATIC FRICTION COEFF.	0.4
DYNAMIC FRICTION COEFF.	0.3

The contact surface analysis reveals a concentration of stresses along the peripheral area of the plate. Additionally, a trend emerges where the soil surface tends to harden, forming a raised feature or protrusion (*Figure 45*).

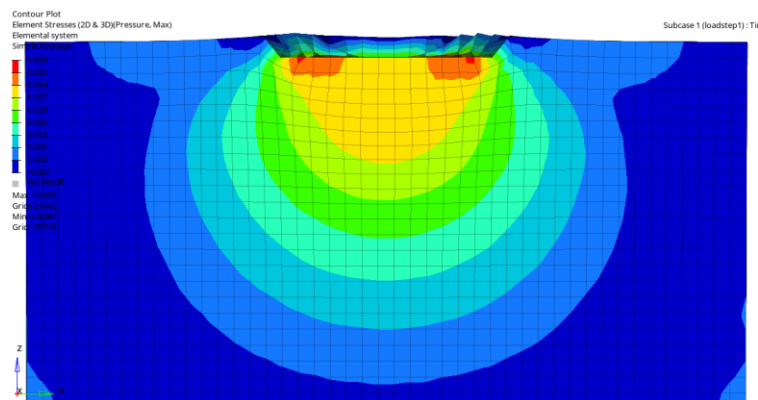


Figure 45: Pressure inside the sample

For the pressure-sinkage characteristic, the study by Ragheb, El-Gindy, and Hossam Kishawy was referenced, providing insights into the development of a pressure-sinkage relationship.

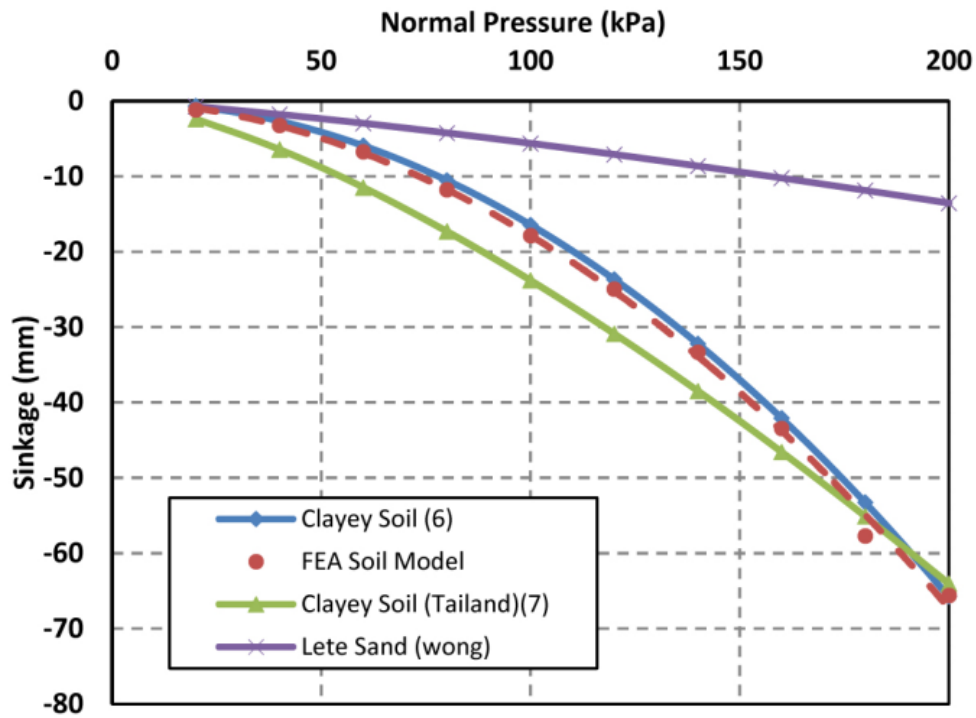


Figure 16. Pressure-sinkage curve for the new soil compared with published data for known soils.

Figure 46: Pressure sinkage, reference paper (Ragheb, El-Gindy, & Kishawy, 2013)

In this initial test, a characteristic response by imposing a sinkage of 10 mm is obtained. Using the data, Bekker's equation (*Equation 1*) was applied, and a fitting procedure is performed to derive the parameter k , which represents the soil stiffness contact for sinkage, and n , a constant related to the soil characteristics.

This approach allowed for a better characterization of the interaction between the footing and the soil by estimating the parameters that govern the soil's response to loading.

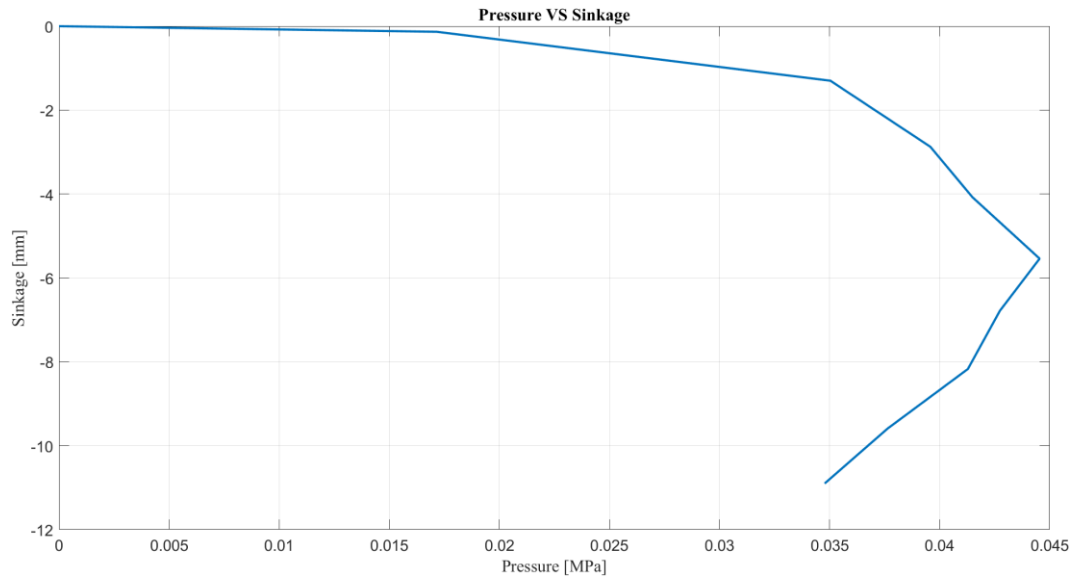


Figure 47: Pressure-Sinkage, with friction

It was observed that performing a fitting allowed for the derivation of a characteristic curve. However, when compared with the reference paper data, it became evident that the imposed sinkage needed to be increased by at least three times, resulting in a sinkage depth of 30 mm.

For the second test, an imposed displacement of 30 mm was applied to the plate. This significantly increased the simulation time, reaching approximately 13 hours.

The trend observed was similar to the previous test, but upon comparing it with the reference paper (Ragheb, El-Gindy, & Kishawy, 2013). It was noted that for the same displacement, the resulting pressure values were approximately one-third lower than those presented in the paper. This suggests that the material properties need to be better defined and refined to improve the accuracy of the model.

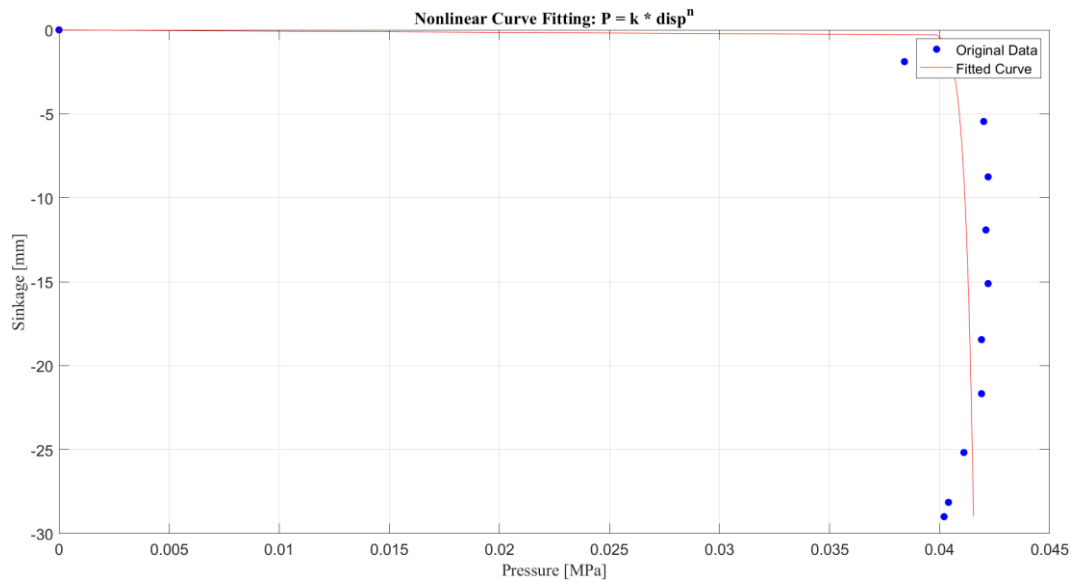


Figure 48: Pressure-Sinkage, 30 mm enforced displacement

As the second iteration of the model, after deriving the initial characteristic, the focus shifted towards geometries more representative of the automotive field. For this reason, a cylindrical geometry simulating a tire was considered, using dimensions comparable to a 205/55 R16 tire (Figure 49).

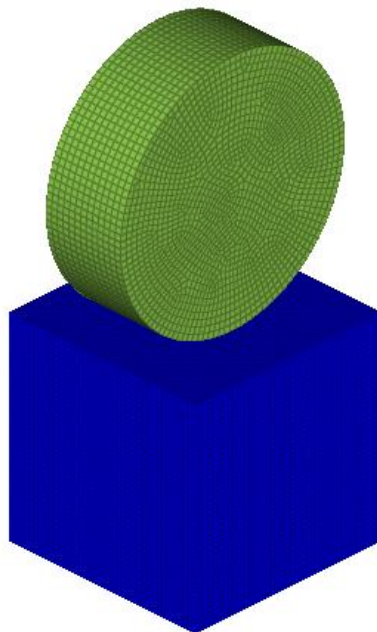


Figure 49: Second iteration model

The properties of the cylinder are detailed in the table below.

Table 17: Cylinder geometry data

D	600	mm
h	200	mm
MESH	15X15	
ELEMENT TYPE	HEXA	

For this iteration, the material properties and constraints were modified. Specifically, the first three degrees of freedom were constrained at all corners of the soil cube. Additionally, the test setup was aligned with previous trials, and loose sand was introduced as the material, with a Young's modulus value of 10 MPa.

These tests were conducted alongside triaxial tests, although the calibrated value of 32 MPa was not yet been verified. The behavior of the material was initially modeled as linear-elastic with perfectly plastic behavior.

As the focus shifted towards the automotive field, a load of 3942 N was applied to the wheel, representing one-quarter of the weight of a 1600 kg C-segment vehicle. In this case, the simulation achieved convergence. However, upon examining the results, it was observed that the material did not reach a state of plasticization. Specifically, when deriving the pressure-sinkage characteristic curve, it was noted that the behavior remained linear.

Additionally, a relatively low displacement of approximately 2.5 mm is measured.

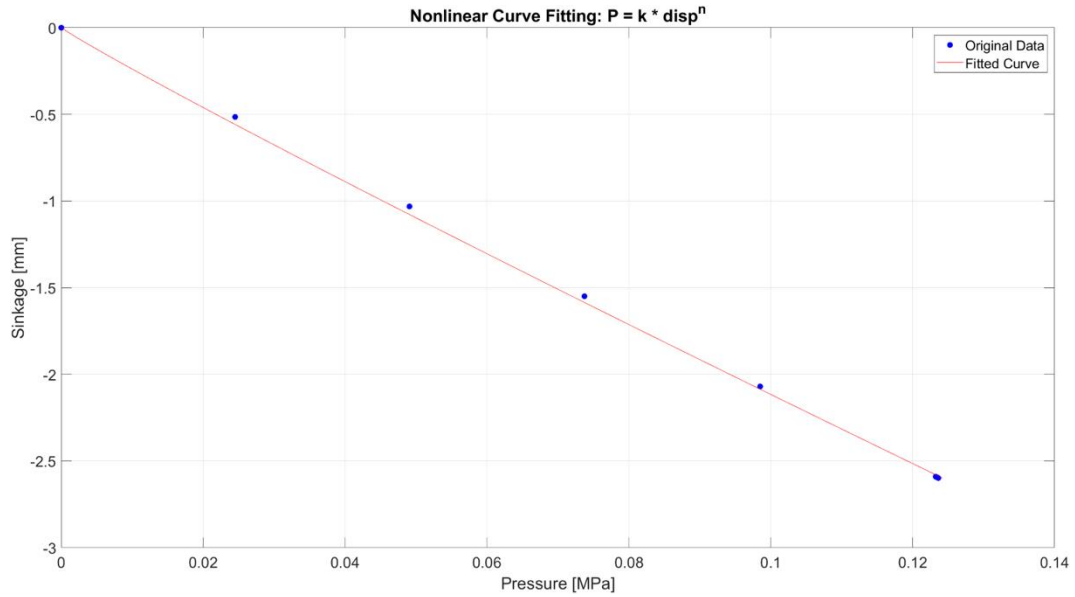


Figure 50: Pressure-Sinkage, with load applied

Furthermore, in attempting to reach the plasticization condition through an increased load, the simulation was unable to achieve convergence.

Analyzing the data revealed that there are still stress concentrations at the edges of the cylinder (Figure 51). This behavior will be addressed in the third iteration of the model by varying the geometry to mitigate these stress concentrations.

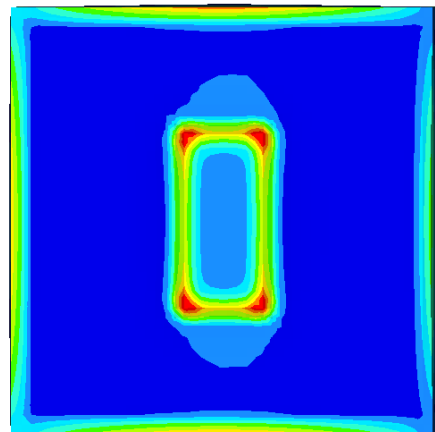
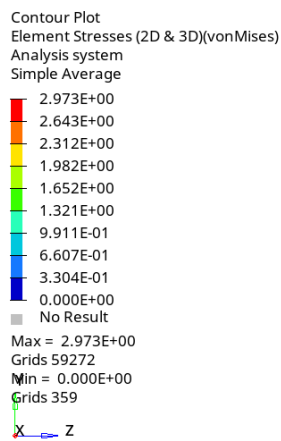


Figure 5128: Top view, stress

In the third iteration of the model, a geometry similar to a tire was introduced, featuring a small fillet radius at the corners to eliminate sharp edges and reduce stress concentrations.

The geometry was imported from the CREO software, and tetrahedral elements were used for meshing.

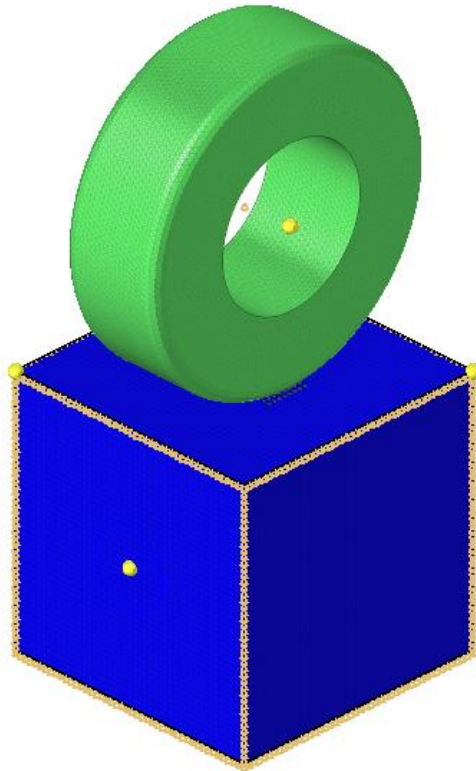


Figure 52: Third iteration model

The properties of the tire are detailed in the table below:

Table 18: Tire model, specification

ELEMENT TYPE	TETRA	
ELEMENT DIMENSION	10X10	mm
TYRE DIAMETER	600	mm
TYRE WIDTH	200	mm
FILLET RADIUS	25	mm

In this case, due to the lack of model convergence and based on the simulation methods and insights gained from previous tests, an enforced displacement of 10 mm was applied. This was combined with a load-unload characteristic, as illustrated in the figure 53.

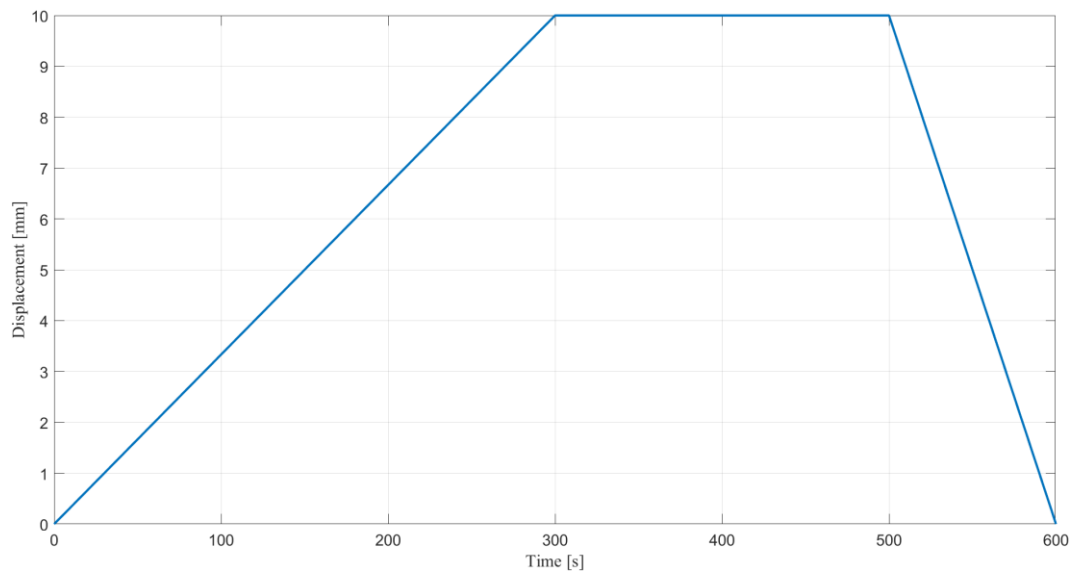


Figure 53: Displacement over time

The enforced displacement was applied to the wheel using a rigid *RB2* element, simulating a motion originating from the wheel hub.

To facilitate model convergence, the displacement was applied very slowly, using a time step *DT* of 0.1 and a total number *N* of 6000 steps, resulting in a simulated duration of 10 minutes.

For the material, a simple modification was introduced: strain hardening was implemented using the parameter *H*. While further investigation of this parameter is warranted, studies indicate that incorporating hardening improves model convergence, as also noted in the previous section.

With the change in geometry and simulation settings, the actual simulation time increased to 48 hours.

By analysing the results, a pressure-sinkage characteristic was derived. Furthermore, in this case, the pressure values were more consistent with those reported in the reference paper, reaching values in the range of kilopascals (kPa).

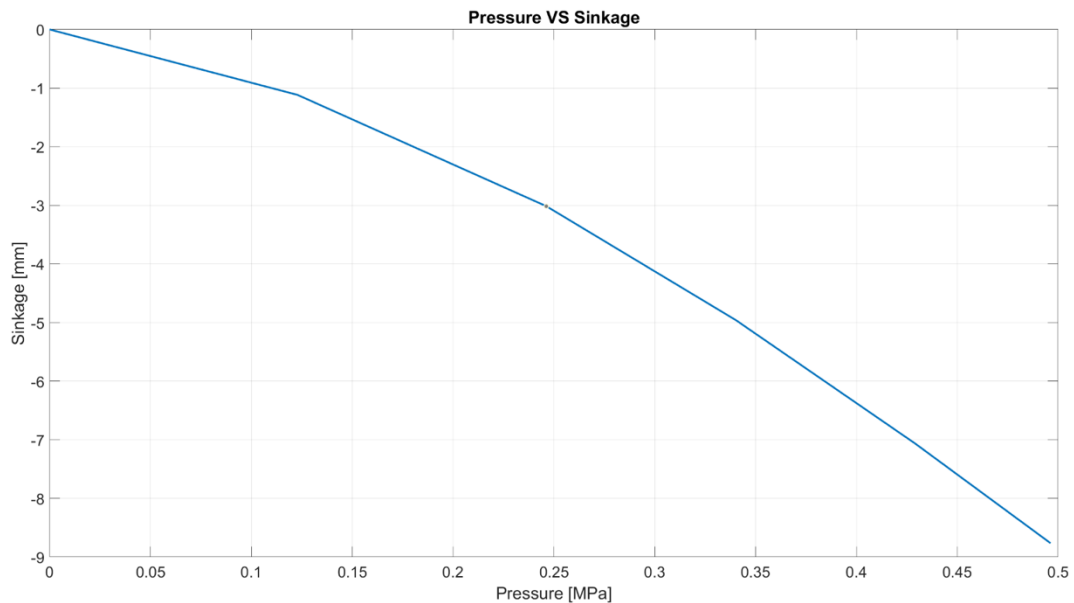


Figure 54: Pressure-Sinkage, Third iteration

Certainly, in this case, it will be necessary to increase the enforced displacement in order to obtain a complete and more accurate characteristic, while still being mindful of the model's convergence. Particular attention must be given to the constraints, which are essential for the correct simulation of the test, but can also be one of the main causes of convergence issues.

Furthermore, as expected, the new geometry has proven to be the best choice. The results obtained, along with the analysis of the stress distribution in the contact area, clearly show that applying a fillet radius to the cylinder significantly reduces the concentration of stresses. This not only facilitates better convergence of the model but also prevents the formation of localized stress peaks that could compromise the reliability of the simulation. The adopted approach thus seems to optimize both the effectiveness and stability of the simulation, confirming the soundness of the geometric choice. (Figure 55).

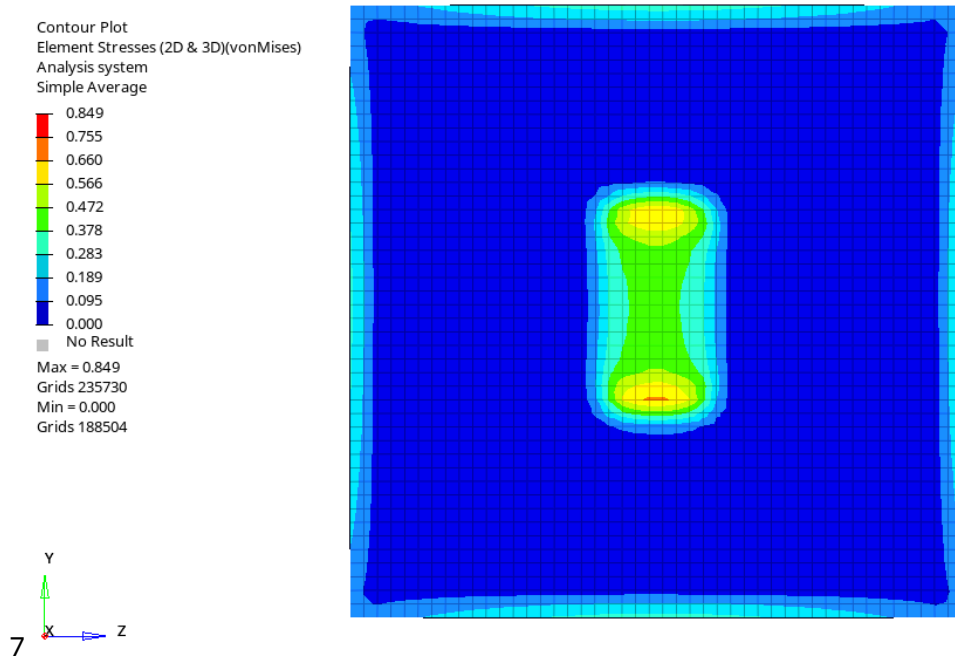


Figure 55: Top view, Stress

Analysing the stress distribution within the system, the formation of a stress bulb (Figure 56) is observed. This behaviour mirrors the trend previously highlighted in the simulation conducted to verify the Boussinesq method in the presence of a plate. Analysing the stress state, it is observed that the maximum stress occurs at the edges of the tire, reaching a value of 1.03 MPa.

Continuing the analysis at a depth of 80 mm, the value obtained from the simulation is compared with the one predicted by the Boussinesq method. The latter leads us to expect a value of 0.412 MPa, while the simulation yields a slightly lower value of 0.342 MPa. Although there is a discrepancy, the simulated value remains close to the theoretical one, confirming a consistency between the results.

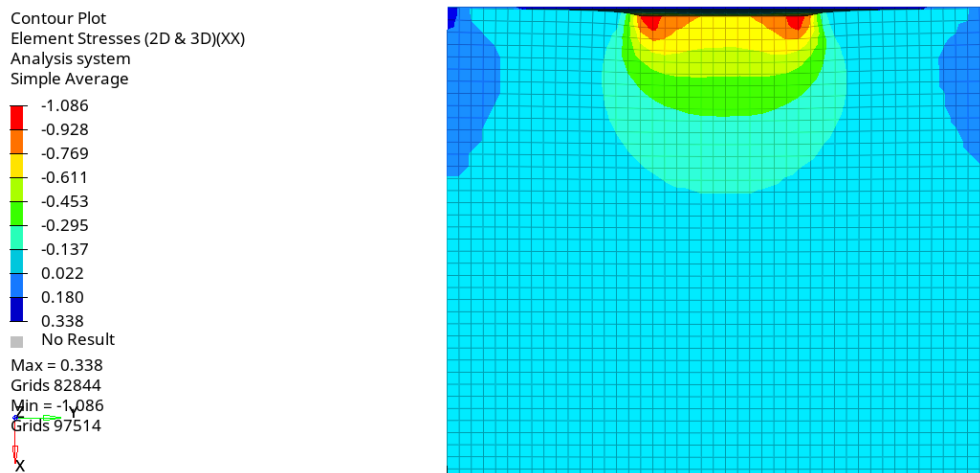


Figure 56: Cut view, tire simulation, axial stress

Analysing the contact patch, a deflection of 10 mm is observed, the contact area measures 155x55 mm. This is relatively small compared to a standard car tire, which typically has a contact patch of approximately 100x200 mm.

5. Conclusion

In conclusion, this study has successfully demonstrated that reproducing the proposed tests is feasible using the selected finite element solver. The findings highlight the solver's capability to provide meaningful results, albeit with a certain degree of approximation when compared to more specialized solvers or software explicitly designed for automotive applications. This discrepancy can be attributed to the inherent general-purpose nature of the solver and the specific requirements of automotive modelling.

Despite these limitations, the study lays a strong foundation for future exploration. By refining the methodology, incorporating advanced modelling techniques, and leveraging the solver's capabilities, it is expected that the precision and reliability of the results will improve significantly. Furthermore, the continued validation of the model against industry-standard benchmarks will provide insights into its performance and potential enhancements.

Expanding the scope of this study could also include exploring alternative configurations, parameter optimizations, and comparisons with experimental data. Such efforts will not only contribute to the refinement of the current approach but also strengthen its applicability in complex automotive simulations, paving the way for broader adoption in related engineering domains.

Considering the resources used for the simulation and the required time, employing a workstation with greater computational power would allow results to be obtained more quickly. Another critical factor affecting simulation time is the number of elements used in the models. For instance, in the pressure-sinkage model, nearly 800,000 solid elements are present, computation times will increase exponentially. However, by reducing the number of elements, simulation times can be significantly decreased, as demonstrated in the case of the triaxial test, where the maximum simulation time was just 45 minutes.

As for future developments, one of the main goals will be to optimize the model in order to reduce simulation times. This is a crucial aspect for the progress of the study, as it would allow for a reduction in the time required to obtain results and accelerate the research process.

Another future development will be the implementation of the Mohr-Coulomb criterion into the current pressure-sinkage model. Since the criterion was introduced in the solver only recently, it will require more testing, as careful attention must be paid to the characteristics of the soil. This will likely increase simulation times, so the first step should be to optimize the calculation times.

Bibliography

- Adamo, F., Andria, G., Nisio, A. D., Lanzolla, A. M., Spadavecchia, M., & Cotecchia, F. (2017). *Development of an automatic system for geotechnical testing*. Turin, Italy: IEEE.
- Aldaoood, A. &. (2022). *Development of a Compressibility Prediction Model Based on Soil Index Properties and Area Under/Bounded by Consolidation and Rebound Curves*. Geotechnical and Geological Engineering.
- Altair OptiStruct Help. (2021). Tratto da https://2021.help.altair.com/2021/hwsolvers/os/topics/solvers/os/mats1_bulk_r.htm
- Consolidation System Front Loading Oedometer. (s.d.). Tratto da GEO-CON Product PTY LTD, test equipment for the construction industry : <https://www.geo-con.com.au/product/consolidation-system-front-loading-oedometer/>
- Fervers, C. (2004). *Improved FEM simulation model for tire–soil interaction*. Journal of Terramechanics.
- GDS instruments. (s.d.). *INTRODUCTION TO TRIAXIAL TESTING*. Tratto da gdsinstruments: <https://www.gdsinstruments.com/>
- Giwangkara, G. &. (2020). Analysis of Internal Friction Angle and Cohesion Value for Road Base Materials in a Specified Gradation. *Journal of Advanced Civil and Environmental Engineering*.
- La Porta, G. (2023). *Artificial Ground Freezing in sandy soils. Experimental and numerical analysis on the role of fine content on the thermo-hydro-mechanical behavior*. PhD thesis Polito.
- Lancellotta, & R. (2012). *Geotecnica*. Zanichelli.
- Laughery, S. &. (1990). *Bekker's Terramechanics Model for Off-Road Vehicle Research*.
- Li, Z., Chen, W., Li, Y., & Wu, W. (2023). *Finite Element Analysis of Tyre Contact Interaction Considering Simplified Pavement with Different Aggregate Sizes*. Applied Sciences.
- Moslem, N., & Hossein, G. (2014). *Numerical simulation of tire/soil interaction*. Iran: Department of Agricultural Machinery Engineering, Faculty of Agriculture,.
- Ragheb, El-Gindy, & Kishawy. (2013). *Development of a Combat Vehicle FEA Tire Model for Off-Road Applications*. SAE Technical Paper.
- Taheri, Sandu, Taheri, Pinto, & Gorsich. (2014). A technical survey on Terramechanics models for tire–terrain interaction used in modeling and simulation of wheeled vehicles. *Journal of terramechanics*.
- Triaxial Test Machine, UU Test System. (s.d.). Tratto da Hira laboratory testing equipment: <https://www.hira.com.tr/En/Product/Triaxial-Test-Machine-Uu-Test-System>

Triaxial testing. (2021, 12 20). Tratto da tephra-seismites: <https://tephra-seismites.com/2021/12/20/triaxial-testing/>

Velling, A. (2020, 06 03). *Stress-Strain Curve*. Tratto da Fractory: <https://fractory.com/stress-strain-curve/>